Joule

CellPress
OPEN ACCESS

Article

Direct imaging of oxygen shifts associated with the oxygen redox of Li-rich layered oxides

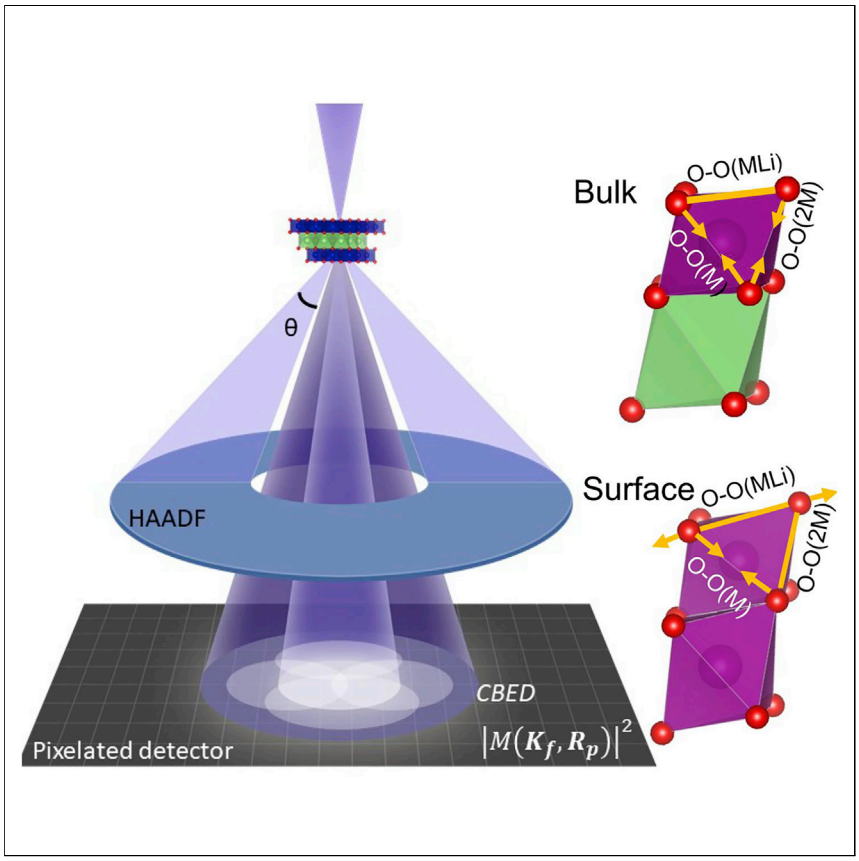

Direct imaging of oxygen distortion in Li-rich metal oxides is key to understand the occurring oxygen redox reaction, whereas this is challenging for conventional atomic-resolution electron microscopy. In this work, we introduce the use of electron ptychography to achieve this and illustrate different oxygen distortions occurring in the bulk and surface of $Li_{1.2}Ni_{0.13}Mn_{0.54}Co_{0.13}O_2$.

Weixin Song, Miguel A. Pérez-Osorio, John-Joseph Marie, ..., Robert A. House, Peter G. Bruce, Peter D. Nellist

weixin.song@materials.ox.ac.uk (W.S.)
peter.nellist@materials.ox.ac.uk (P.D.N.)

Highlights

Electron ptychography enables O and Li imaging in metal oxides

Picometer-scale precision measurement shows oxygen deformation

Oxygen shift in charging cannot recover after discharge explaining hysteresis

Altered oxygen sublattice after first cycle changes the cycling voltage profiles

Song et al., Joule 6, 1049–1065
May 18, 2022 © 2022 The Author(s). Published by Elsevier Inc.
https://doi.org/10.1016/j.joule.2022.04.008

Joule

CellPress
OPEN ACCESS

Article

Direct imaging of oxygen shifts associated with the oxygen redox of Li-rich layered oxides

Weixin Song,[1,2,3,*] Miguel A. Pérez-Osorio,[1,2,3] John-Joseph Marie,[1,2,3] Emanuela Liberti,[1] Xiaonan Luo,[1] Colum O'Leary,[1] Robert A. House,[1,2,3] Peter G. Bruce,[1,2,3] and Peter D. Nellist[1,2,3,4,*]

SUMMARY

Li-rich metal oxides, such as $Li_{1.2}Ni_{0.13}Mn_{0.54}Co_{0.13}O_2$, can deliver high specific capacities because of the redox of lattice O^{2-} in addition to the cations. Observing oxygen distortions is key to understand the redox process. Electron ptychography is a phase-reconstruction method in 4D scanning transmission electron microscopy, providing atomic-resolution phase images with high signal-to-noise ratio and dose efficiency. Herein, we use electron ptychography to image the oxygen shift in $Li_{1.2}Ni_{0.13}Mn_{0.54}Co_{0.13}O_2$ during the first cycle. The picometer-scale precision measurement shows distinct oxygen shifts in the bulk and surface after charging and compares with various theoretical anionic redox models. The shift after discharging is not seen to recover in the bulk accounting for voltage hysteresis; however, it recovers close to the surface, although with a phase change. We suggest that $Li_{1.2}Ni_{0.13}Mn_{0.54}Co_{0.13}O_2$ proceeds distinct oxygen redox in the bulk and surface. The altered oxygen sublattice after first cycle potentially explains the changed voltage profiles of following cycles.

INTRODUCTION

Li-rich layered metal oxides, such as $Li_{1.2}[Ni_{0.13}Mn_{0.54}Co_{0.13}]O_2$, offer specific capacities exceeding 250 mAh g^{-1} in Li-ion batteries (LIBs)—much higher than the conventional layered oxides such as $Li[Ni_xCo_yMn_z]O_2$, 160–210 mAh g^{-1} for x = 0.33–0.85.[1,2] The high specific capacity of Li-rich metal oxides results from the redox reaction of both transition-metal (TM) cations and oxygen anions that compensates the charges in the de- and reintercalation of Li^+ ions, unlike conventional oxides that rely on solely cationic redox. Oxygen redox has been evidenced in Li-rich *3d*-, *4d*-, and *5d*-metal oxides both theoretically and experimentally.[1] Among these oxides, *3d*-oxides are highly promising for commercialization because of their low cost and weight. $Li_{1.2}[Ni_{0.13}{}^{2+}Mn_{0.54}{}^{4+}Co_{0.13}{}^{3+}]O_2$ is one promising candidate, and it delivers a reversible specific capacity above 250 mAh g^{-1} associated with the redox reaction of $Ni^{2+/4+}$, $Co^{3+/4+}$, and O^{2-} ions.[3] Although a high specific capacity is delivered, $Li_{1.2}[Ni_{0.13}Mn_{0.54}Co_{0.13}]O_2$ suffers from voltage hysteresis,[4,5] sluggish kinetics,[6,7] and voltage fading in cycling,[8,9] leading to poor performance in the energy efficiency, power capability, and cycling stability, respectively. These issues predominantly observed in Li-rich cathodes have been suggested to be associated with the oxygen redox. A number of models for the oxidized O^{2-} product have been proposed to explain this impact of oxygen redox, including pinned hole states on the oxygen sublattice,[10] formation of O_2 molecules,[11] or peroxo-like species ($O_2{}^{n-}$, n = 1, 2, or 3).[7,12] Recent studies[10,11] suggest that the voltage hysteresis is driven by in-plane TM migration, formation of vacancy clusters, and trapped O_2

Context & scale

Li-rich metal oxides deliver larger specific capacities in Li-ion batteries than conventional oxides resulting from the redox of lattice O^{2-} ions and cations, although they suffer from the voltage hysteresis and degradation of the voltage and capacity. Atomic-resolution imaging on the structural evolutions of Li-rich oxides in oxygen redox is critical to understand the problems. Imaging oxygen distortion is particularly important, but in conventional electron microscopy is challenging to achieve. Here, we use an advanced 4D scanning transmission electron microscopy technique, namely electron ptychography, to image the oxygen shift in an archetypal $Li_{1.2}Ni_{0.13}Mn_{0.54}Co_{0.13}O_2$ upon the first charge-discharge cycle. Our picometer-scale precision measurement points out distinct oxygen shifts in the bulk and surface regions, implying different redox mechanisms. We believe that the results of oxygen shifts aid the building of understandings on oxygen redox and the associated problems.

This is an open access article under the CC BY license (http://creativecommons.org/licenses/by/4.0/).

molecules in the vacancy clusters. Suppressing in-plane TM migration inhibits O_2 formation and avoids voltage hysteresis.[10] Such understanding correlates the oxygen redox with the irreversible loss of first-charging plateau and the structural changes arising from TM migration; however, the oxygen sublattice distortion process has not been directly observed during the redox processes. Observing the coordination of cations by O is crucial to the comprehensive understanding of oxygen redox.

Transmission electron microscopy (TEM) is an imaging technique providing atomic-scale structural information of samples. However, imaging light elements, such as oxygen and lithium, is challenging because they only weakly scatter the electrons, resulting in a small shift in the transmitting electron wave phase. Additionally, the cathode materials investigated here are highly susceptible to damage under the electron irradiation. Conventional high-resolution TEM is able to image these phase shifts, but the atoms are difficult to distinguish between Li, O, and TMs because of the complex dependence of the image contrast on atomic number, lens aberrations, and sample thickness. High-angle annular dark field (HAADF) imaging in scanning TEM (STEM) is sensitive to the atomic species because the contrast is approximately proportional to the square of the atomic number, *Z*. However, oxygen atoms have a low *Z* and a very low contrast. The small contrast of oxygen is usually invisible in the HAADF images of metal oxides because the strong contrast of nearby heavier TMs overshadows that of oxygen. To simultaneously image the heavy and light atoms, several imaging techniques have been developed. Annular bright field (ABF) imaging can image light atoms by integrating the scattered signals over an ABF detector but requires lens aberrations or multiple scattering to generate phase contrast[13] and is not tolerant to the sample mistilt.[14] Coherent bright field (BF) STEM imaging offers phase contrast but detects a small fraction of the scattered electrons and is not sufficiently efficient for these beam-sensitive materials. Differential phase contrast (DPC) and integrated DPC (iDPC) can form dose-efficient phase-contrast images[15] but can be susceptible to lens aberration effects when very precise measurements are required.

Electron ptychography is a method to reconstruct the phase contrast of the specimen from 4D datasets formed by the 2D probe positions in raster scanning and the 2D convergent beam electron diffraction (CBED) patterns recorded at each probe position. The datasets are collected in a 4D STEM geometry (Figure 1A) where a pixelated detector is used to record the CBED patterns at a high speed. The ptychographic phase image retrieved from the 4D datasets is sensitive to both heavy and light elements and can improve the spatial resolution over the usual diffraction limit.[16] Electron ptychography has a simple contrast transfer function and inherently filters the image noise without sacrificing the signal strength and allows for the correction of any residual optical aberrations, resulting in a high signal-to-noise ratio.[17] This method processes the scattered electrons from the entire BF region and thus has higher dose efficiency than other imaging modes that only collect a fraction of the scattered electrons over a particular angular range.[18,19] The high efficiency in dose and contrast transfer allows to minimize the beam currents to sub-pA, highly reducing the beam damage. Electron ptychography does not require lens aberration to form contrast; thus, an aberration-free HAADF image can be recorded simultaneously. Both the phase and ADF images can identify the locations of the heavy and light atoms. The numerical correction of aberrations further reduces the beam damage by minimizing the sample exposing time in the microscope since precise adjustment of the electron optics is not required. Ptychography also allows retrieval of 3D structural information through optical sectioning.[13] Simultaneous

[1]Department of Materials, University of Oxford, Oxford OX1 3PH, UK

[2]The Faraday Institution, Didcot OX11 0RA, UK

[3]The Henry Royce Institute, Oxford OX1 3PH, UK

[4]Lead contact

*Correspondence:
weixin.song@materials.ox.ac.uk (W.S.),
peter.nellist@materials.ox.ac.uk (P.D.N.)

https://doi.org/10.1016/j.joule.2022.04.008

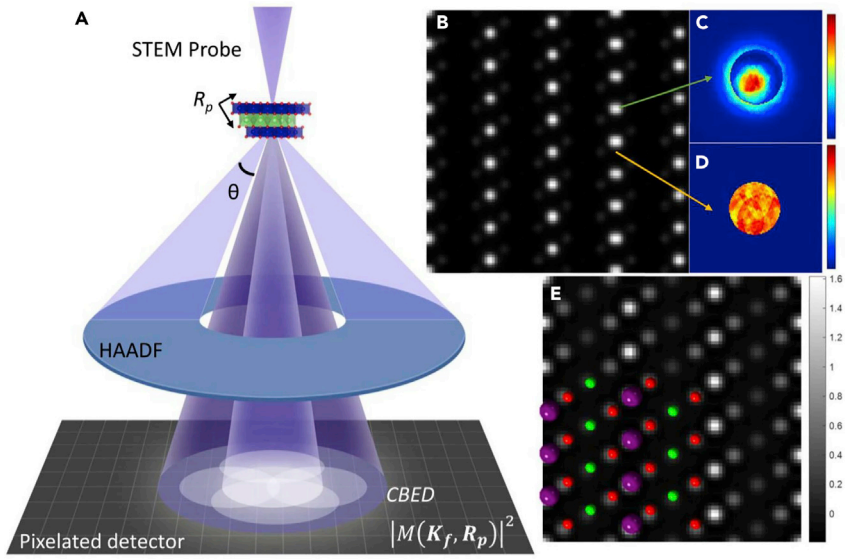

Figure 1. Scheme of electron ptychography and simulated images of $Li_{1.2}[Ni_{0.13}Mn_{0.54}Co_{0.13}]O_2$

(A) 4D STEM geometry with a focused STEM probe. The probe is in a 2D raster scan, forming 2D CBED patterns on the detector plane, K_f, at each probe position, R_p. The intensity of the electron wave function, $|M(K_f, R_p)|^2$, is recorded by a pixelated detector.

(B) Simulated ADF image of $Li_{1.2}[Ni_{0.13}Mn_{0.54}Co_{0.13}]O_2$ along [010] $_{monoclinic}$ zone axis.

(C and D) CBED patterns at two different R_p showing distinct intensity. The color bars are in the same scale.

(E) Ptychographic phase image reconstructed by the Wigner distribution deconvolution (WDD) algorithm, displaying the contrast from heavy metals and light oxygen and lithium atoms. The grayscale bar is in radians. The atomic model is superimposed in (E) where purple spheres are transition metals, red are oxygen and green are lithium atoms.

ptychographic phase and HAADF images from a same local structure enable precise identification of oxygen and measurement of the oxygen distortion in the structure.

In this work, we directly imaged the oxygen shift in a typical 3*d* metal oxide, $Li_{1.2}[Ni_{0.13}Mn_{0.54}Co_{0.13}]O_2$, during the first cycle. The distortion is determined by the measurement of the projected atom distance in cycling with a picometer-scale precision. We show different oxygen distortions in the bulk and surface regions of $Li_{1.2}[Ni_{0.13}Mn_{0.54}Co_{0.13}]O_2$ after charging. It is found that the distorted oxygen sublattice cannot fully recover to the pristine situation in the bulk material even after discharging, accounting for the first-cycle voltage hysteresis. The oxygen sublattice formed after the first cycle is different from that of the pristine state, leading to altering local environment of TMs and Li and voltage profiles in subsequent cycles.

RESULTS AND DISCUSSION

Simultaneous ADF and ptychographic imaging

Figure 1A schematically shows the 4D STEM geometry with a focused probe. A raster scanning of the probe on the sample results in a 2D set of probe positions, R_p. At each R_p, a 2D CBED pattern is generated and collected by the fast pixelated detector, such that the whole CBED pattern from each of the probe positions can be recorded. In a CBED pattern, the intensity at each pixel of the detector plane, K_f, is the square of the amplitude of the exit wave function, M(K_f, R_p). The 2D probe positions and 2D diffraction patterns form the so-called 4D STEM dataset. To explain the phase reconstruction using electron ptychography from the 4D datasets, we use simulated datasets of $Li_{1.2}[Ni_{0.13}Mn_{0.54}Co_{0.13}]O_2$ with a 2 nm thickness along

$[010]_{monoclinic}$ projection using the multislice approximation theory.[20] Figure 1B shows the simulated ADF image of $Li_{1.2}[Ni_{0.13}Mn_{0.54}Co_{0.13}]O_2$ where the TM atoms are identified resulting from the strong contrast $\sim Z^{1.6-1.8}$. The light O and Li atoms have a low Z number, thus a weak contrast and become invisible when close to the TM atoms because of the overwhelming contrast of the high-Z TM atoms. In the scanning of the sample, CBED patterns at each probe position have varying intensity. Figures 1C and 1D display two different CBED patterns. The recorded intensity is the modulus square of the exit wave function $|M(K_f, R_p)|^2$ such that the phase information is lost. To retrieve the phase, we perform ptychographic reconstruction to obtain the exit wave function. A complex 4D dataset, $G(K_f, Q_p)$, is generated by Fourier transformation of $|M(K_f, R_p)|^2$ with respect to R_p, where Q_p is the conjugate spatial frequency. High-quality phase information is retrieved from the interference of the direct and first-order diffraction beam in the diffracted disc-overlap regions. The image is formed through a ptychographic reconstruction that inherently filters nonoverlapped regions and helps reduce the electron counting or Poisson noise.[18] One algorithm of ptychographic phase reconstruction is Wigner distribution deconvolution (WDD) that is relatively robust to the sample thickness.[13] Figure 1E shows the WDD phase image from the same sample area in Figure 1B. In such phase image, both the heavy TMs and light O and Li atoms are visible. The locations of TMs are identifiable referring to the atom positions in the simultaneous Z-contrast HAADF image, enabling the atomic pattern of ptychographic phase image to be directly interpretable. Furthermore, the 4D STEM datasets used for ptychographic phase reconstruction allow forming virtual images of different imaging modes, such as BF, ABF, and DPC through data processing, see Figure S1.

Figures 2A and 2B display the HAADF and WDD phase images of the layered structure of $Li_{1.2}[Ni_{0.13}Mn_{0.54}Co_{0.13}]O_2$, respectively, the data for which are recorded simultaneously. In the HAADF image, only the contrast from TMs is shown, although the phase image also displays the contrast from the light O and Li. TMs at the outmost surface of the particle (bottom right) are invisible in the HAADF image because of the small thickness and resulting low contrast from this region but are clearly revealed in the phase image. Such high sensitivity to the atoms in the ptychographic phase image is due to the high-contrast transfer and dose efficiency of electron ptychography.[13,18,21] In the WDD phase image, TMs, O, and Li atoms are unambiguously identified using the simultaneous HAADF identifying the TMs positions and enables direct measurement of the atom distances between the various atomic species. To distinguish the distances along various directions, we name three distances between the TMs atoms: M–M, M–M(OLiO), and M–M(Li); three types of O–O projection in $[TMO_6]$ octahedra: O–O(M), O–O(2M), and O–O(MLi); and two types in $[LiO_6]$ octahedra: O–O(Li) and O–O(2Li), illustrated in Figure 2C. The red lines crossing the TM atoms, of which the center of mass is determined by StatSTEM software,[22] in the HAADF and WDD phase image are along the M-M(OLiO)/O–O(Li) orientation. The line intensities are fitted using cubic smoothing spline interpolation, and the obtained spline profiles (Figure 2D) optimize the peak positions of TMs, O, and Li atom columns. The spacing between the TM columns is the projected M–M(OLiO) distance and between O is the projected O–O(Li) distance that is averaged over the sample thickness.

Increasing the number of measurements produces statistics of the atom distances that are more representative than a single measurement from a local area. The number of measurements is the total number of events in the histogram of atom distance that was used to calculate the mean and error. Precise measurement of the atom distances is required to reveal the O shift in $Li_{1.2}[Ni_{0.13}Mn_{0.54}Co_{0.13}]O_2$.

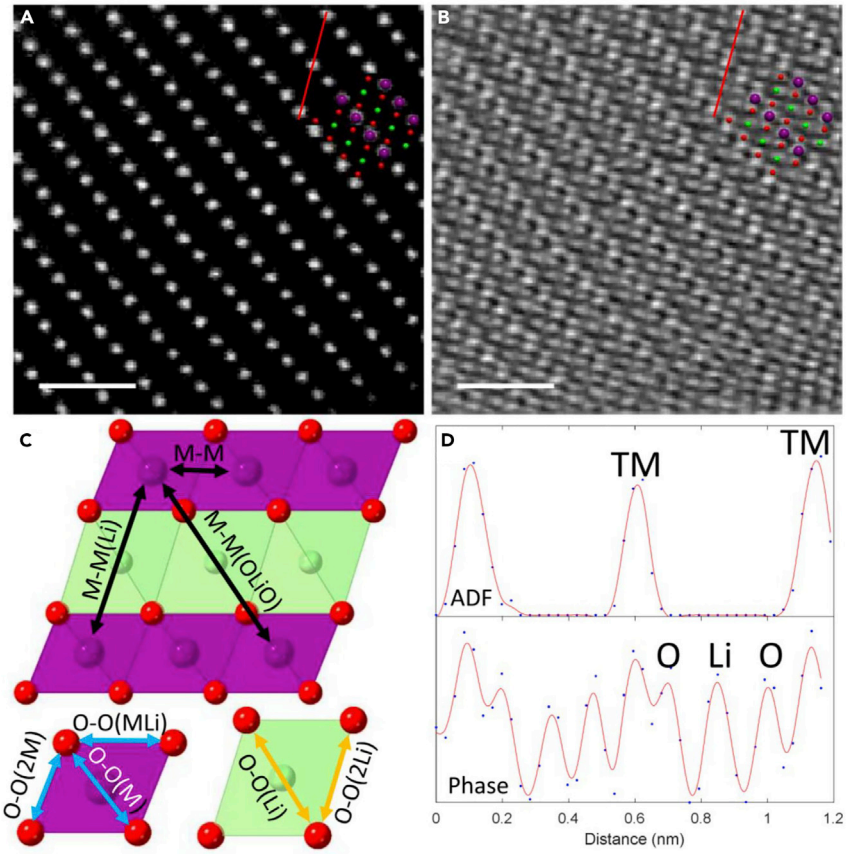

Figure 2. Measurement of the projected atom distance from $[010]_{monoclinic}$ zone axis of $Li_{1.2}[Ni_{0.13}Mn_{0.54}Co_{0.13}]O_2$

(A and B) (A) HAADF and (B) WDD phase image along $[010]_{R\text{-}3m}$ projection at a dose of 2.9×10^4 $e^-/Å^2$. HAADF image is simultaneously recorded with the 4D STEM datasets. The atomic model is superimposed. Purple is TM, red is O, and green is Li. Scale bar is 1 nm.

(C) Illustration of the named atom distances in TMO_6 (purple) and LiO_6 (green) octahedra. Atom types in the brackets of the names indicate nearby species to the midpoint of the projected bond. O–O(M) is the equatorial O–O projection, O–O(MLi) is projection of O–O bonds parallel to TM plane, and O–O(2M) is the projection of out-of-plane O-O bonds. O-O(Li) is the equatorial O–O projection in alkali layers and O–O(2Li) is out-of-plane projection.

(D) Line profiles across the red lines from the HAADF and WDD phase images. The phase image points out locations of Li and O where absent in the line profiles from the HAADF image.

Sample drift and beam damage are always present in high-resolution STEM imaging. Both issues are exacerbated in 4D STEM because of the much longer dwell time. We initially performed multiframe fast acquisition of HAADF images using SmartAlign,[23] which uses a very small dwell time to fractionate the dose across several images—an approach that has also been seen to reduce sample damage[24]—prior to the acquisition of the ptychography data. The postprocessing of the multiframes using rigid and nonrigid registration algorithms form high signal-to-noise ratio and zero-drift HAADF images.[23] The TM-TM distances from the zero-drift HAADF images can then be used to calibrate the distances in the phase image. The difference ratio is used to calibrate the O–O distances along the same orientation as the particular TM–TM distance. An example of the calibration procedure in the bulk region is shown in Figures S2 and S3. Changes in the statistically analyzed O–O projected distance can reveal how the O shifts and how the $[TMO_6]$ octahedra distort at different stages of cycling.

In the voltage profiles of $Li_{1.2}[Ni_{0.13}Mn_{0.54}Co_{0.13}]O_2$ (Figure S4), the first cycle shows large voltage hysteresis and difference from the following cycles. The charging plateau before 4.5 V versus Li^+/Li is associated with the oxidation of Ni^{2+}/Co^{3+} to Ni^{4+}/Co^{4+} and the plateau at 4.5 V versus Li^+/Li results from lattice O^{2-} oxidation.[9,25,26] The subsequent discharge curve shows a typical S-shape slope associated with the reduction of the tetravalent TMs and trapped oxygen molecules[11] at a lower average voltage compared with charging. Such large variation in the redox potentials is associated with the change in the local environments of TMs and O. To understand the oxygen shift and $[TMO_6]$ distortion in the first cycle, we studied the charged sample at a cutoff of 4.6 V versus Li^+/Li and discharged sample at 2 V versus Li^+/Li, respectively. To evidence the consistency in the measured atom shift of $Li_{1.2}[Ni_{0.13}Mn_{0.54}Co_{0.13}]O_2$ at specific cycling stages, at least two samples were studied in each stage, and the results are shown in Figures S6–S17 and S21–S26. We now consider these results for the bulk and surface regions of the cathode material.

Distinguishing bulk and surface structure change

Figures 3A, 3D, and 3G show the zero-drift HAADF images of $Li_{1.2}[Ni_{0.13}Mn_{0.54}Co_{0.13}]O_2$ at pristine, charged and discharged states obtained from multiframe scanning with doses of 3,720, 2,050, and 1,943 $e^-/Å^2$ in each frame, respectively. At such a dose, the layered structure is clearly seen in the pristine sample with the absence of visible contrast from the alkali layers. In contrast, the HAADF images of charged and discharged samples all display reconstructed cubic layers (in spinel-like/rocksalt phase) within ~2 nm thickness from the surface after charging and extending to ~4 nm after discharging, in line with previous results.[11,27] High electron dose has been reported to exacerbate out-of-plane TM migration and lead to surface layer reconstruction.[28] The charged samples, containing highly oxidized TMs are particularly sensitive to the beam damage. In this work, the used dose for electron ptychography is in a magnitude of $\sim 10^4$ $e^-/Å^2$. To evaluate the beam damage of such dose levels, we compared the ADF images of charged $Li_{1.2}[Ni_{0.13}Mn_{0.54}Co_{0.13}]O_2$ sequentially collected at a dose of 8.1×10^4 $e^-/Å^2$ per frame. Figure S5 shows the images, of which the surface cubic layers maintain a ~2 nm thickness, even in the second frame with an accumulated dose of 1.6×10^5 $e^-/Å^2$. This result indicates that the dose of 8.1×10^4 $e^-/Å^2$, which is close to that used for electron ptychography, has not induced huge beam damage to the sample even at charged states.

The reconstructed layer forms only in a ~4 nm thickness region over the surface of $Li_{1.2}[Ni_{0.13}Mn_{0.54}Co_{0.13}]O_2$ in the first cycle, although the regions beyond still maintain the layered structure, indicating the phase change is depth dependent. To distinguish the regions with and without phase change in the first cycle, we treat the regions within 4 nm of the sample edge as surface and the regions beyond 5 nm as the bulk when considering limited fields of view when performing electron ptychography. The optical sectioning effect of ptychography enables direct imaging of the bulk structure at specific depths excluding the distortions from the surface,[29] although the surface phase always contributes to the ADF images projected over the average of a large depth. We start by discussing the structural changes in the bulk region in the first cycle.

Bulk oxygen shift in TM/O redox

Figures 3B, 3C, 3E, 3F, 3H, and 3I display the simultaneous HAADF and WDD phase images of the bulk region in pristine, charged and discharged $Li_{1.2}[Ni_{0.13}Mn_{0.54}Co_{0.13}]O_2$, respectively. The TMs are located at octahedral sites in a cubic close-packed (ccp) oxygen sublattice. As described earlier, the TM distances are accurately measured from aligned multiple HAADF images (Figures S6–S11) and are used to calibrate the

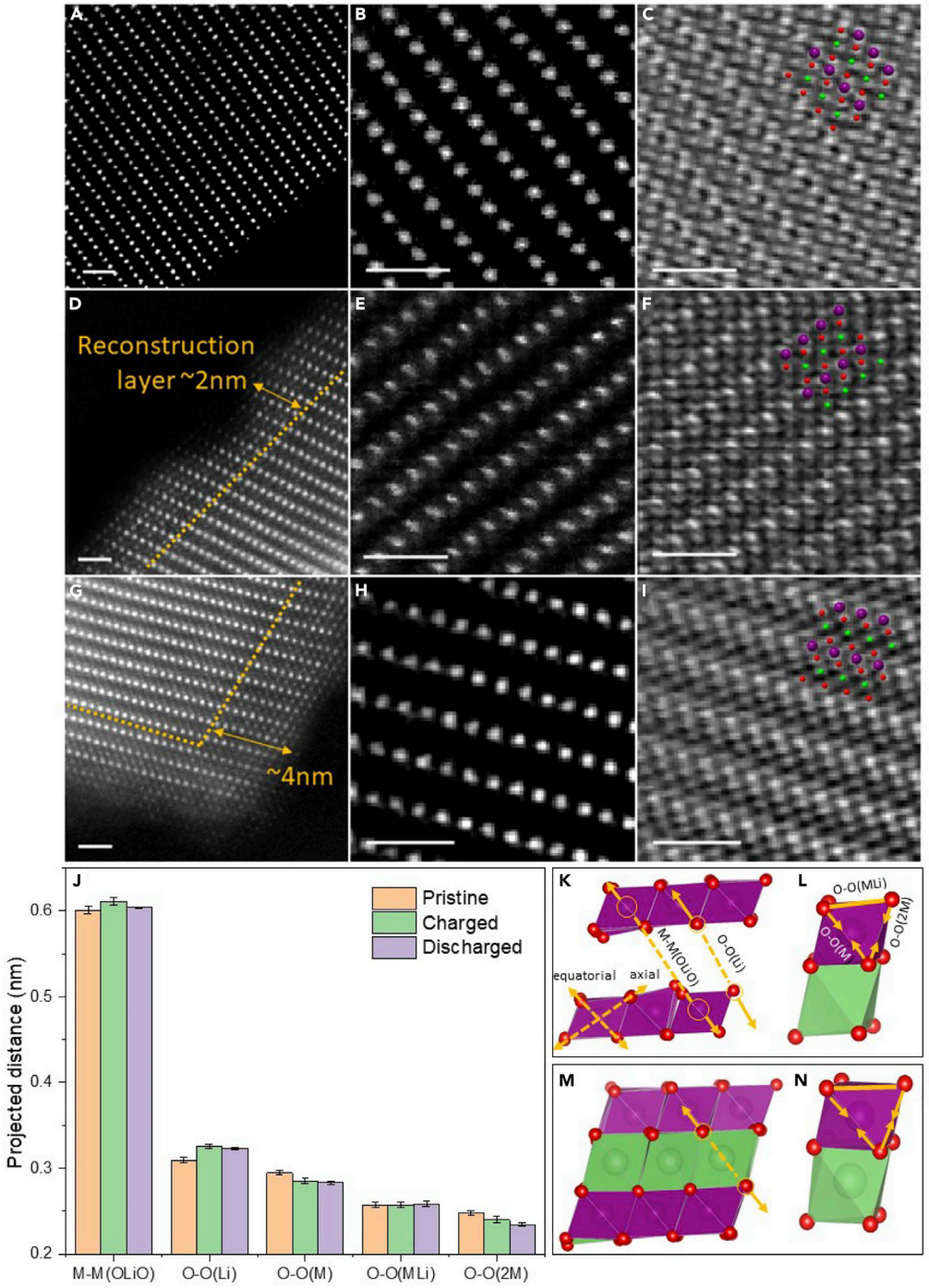

Figure 3. Atomic-resolution images of the layered structure of $Li_{1.2}[Ni_{0.13}Mn_{0.54}Co_{0.13}]O_2$ projected along $[010]_{monoclinic}$ zone axis

(A–I) (A–C) Pristine state. (D–F) Charged state to 4.6 V versus Li^+/Li. (G–I) Discharged state to 2 V versus Li^+/Li. (A, D, and G) Multiframe registered HAADF images to reduce scanning drift and mitigated beam damage. The electron doses of (A, D, and G) are 3×10^4, 1.6×10^4, and 1.5×10^4 $e^-/Å^2$, but in each frame, (8 frames in total) were 3,720, 2,050, and 1,943 $e^-/Å^2$, respectively. (B, E, and H) HAADF images of the bulk region and corresponding. (C, F, and I) WDD phase image reconstructed from the simultaneously recorded 4D datasets. The doses in (B and C), (E and F), and (H and I) are 8.7×10^4, 8.1×10^4, and 8.3×10^4 $e^-/Å^2$, respectively. Superimposed in (C, F, and I) is the atomic model where purple is TM, red is oxygen, and green is Li. Scale bar in all images is 1 nm.

(J–N) (J) Bar chart of the atom distances. The left two, M–M(OLiO) and O–O(Li), relate primarily to the interlayer space, and the right three O–O distances represent $[TMO_6]$ octahedra—O–O(M) and O–O(2M) are out-plane octahedral distance, whereas O–O(MLi) is in-plane distance. Schematic

Figure 3. *Continued*
displacement vectors of the (K and M) layer spacing and (L and N) TMO_6 octahedra at (K and L) charged and (M and N) discharged states compared with the pristine state. Purple and green octahedra represent [TMO_6] and [LiO_6], respectively. The axial and equatorial O–O directions of [TMO_6] octahedra are shown in (K).

ptychographic images from which the remaining atomic distances are measured (Figures S12, S14, and S16). The reproducibility of the results is evidenced through the measurement of a second sample particle (Figures S13, S15, and S17) that gives results consistent within the computed error. The results of the measurements are shown in Table 1 (with a full list in Tables S1–S3) and Figure 3J. The error presented is the standard error of the mean and demonstrates picometer-scale precision.

Starting with the interlayer distances that traverse the alkali layer, it can be seen that on charging, the M–M(OLiO) and O–O(Li) distances (Figure 3K) increase by 1.7% and 5.1%, respectively. The layer expansion results from the enhanced electrostatic repulsion of oxygen layers after Li de-intercalation from the alkali layer[26] and excludes the possibility of oxygen dimerization across the alkali interlayer. The 1.7% increase of M–M(OLiO) is statistically significant and consistent with the increase of *c* cell parameter from 1.42 to 1.44 nm by 1.4% evidenced by the *in situ* X-ray diffraction studies.[26]

The much larger fractional increase in the O–O(Li) distance on charging compared with the M-M(OLiO) increase demonstrates a considerable contraction of TM–O distances in the [TMO_6] octahedra. This effect is also seen in the contraction of the O–O(M) equatorial octahedral distance by 3.2% and is explained by the shrinking TM–O bonds after TM oxidation, leading to contracted ionic radii and increased bond covalency in oxygen oxidation.[26,30] The O–O(2M) distance also decreases by a similar fraction of 3.3%, but the O–O(MLi) length, lying parallel to the layer, remains unchanged by charging. The resulting [TMO_6] octahedra, schematically shown in Figure 3L, are contracted and distorted compared with the pristine material. We note that the O–O(2M) octahedral edges shared by two adjacent [TMO_6] octahedra show the greatest response to oxidation on charging.

Recent studies[11] using resonant inelastic X-ray scattering and ^{17}O magic angle spinning NMR spectroscopy suggest that O_2 molecules are formed in the O^{2-} oxidation of $Li_{1.2}[Ni_{0.13}Mn_{0.54}Co_{0.13}]O_2$. To illustrate how the measured data presented here may be used, we performed density functional theory (DFT) modeling with O_2 molecules formed in the TM vacancies after oxidation. The charged DFT model in Figure S18 is simulated with four vacancy clusters and two molecular O_2 trapped in the TM layers (referred to here as DFT_O_2). Such a model has a higher stability compared with the model of removing the trapped O_2 from the vacancies (referred to here as DFT_V_{O2} and shown in Figure S19C), which has a 200 meV per formula unit (f.u.) higher formation energy than the DFT_O_2 model. Another two alternative DFT models of charged $Li_{1.2}[Ni_{0.13}Mn_{0.54}Co_{0.13}]O_2$ were calculated (Figures S19B and S19C) by considering electron holes formed and localized on the oxygen anions that coordinated with two TMs in the honeycomb structure[11] (referred to here as DFT_hole) and only Co^{3+}/Ni^{2+} cation oxidation (referred to here as DFT_TM). The projected distances in the charged models and changes relative to the results in the DFT model of pristine $Li_{1.2}[Ni_{0.13}Mn_{0.54}Co_{0.13}]O_2$ are listed in Tables S4–S7.

Table 2 summarizes the changes in the atom distances of $Li_{1.2}[Ni_{0.13}Mn_{0.54}Co_{0.13}]O_2$ from the pristine to oxidized state, obtained from experimental measurements and compares them with predictions by the three DFT models of charged

Table 1. Mean atom distances in $Li_{1.2}[Ni_{0.13}Mn_{0.54}Co_{0.13}]O_2$ from a bulk region after drift calibration

Bulk region		Pristine	Charged	Δ(Charge-pristine)	Discharged	Δ(Discharge-pristine)
TMO_6	O-O(M)	0.295 ± 0.002	0.285 ± 0.003	−3.2%	0.283 ± 0.002	−4.0%
	O-O(MLi)	0.257 ± 0.003	0.257 ± 0.003	0	0.258 ± 0.003	0.6%
	O-O(2M)	0.248 ± 0.002	0.240 ± 0.004	−3.3%	0.234 ± 0.002	−5.6%
Layers	M-M(OLiO)	0.601 ± 0.004	0.611 ± 0.004	1.7%	0.604 ± 0.001	0.5%
	O-O(Li)	0.309 ± 0.003	0.325 ± 0.003	5.1%	0.323 ± 0.002	4.3%

The results are measured from pristine, first-charged and first-discharged states. The units are all nm. The difference (Δ) after charging and discharging is relative to the pristine state.

$Li_{1.2}[Ni_{0.13}Mn_{0.54}Co_{0.13}]O_2$. The changes and relative change of O–O(Li)/M–M(OLiO) from experimental measurements are overall more consistent with the results of the atom shift with the DFT model of forming O_2 molecules that are trapped in TM vacancy clusters, compared with the other two models forming electron holes and proceeding pure TM oxidation, although the measurements of the octahedral distortion are somewhat smaller in magnitude. Direct imaging of such vacancy clusters and O_2 molecules is challenging because of the signal to noise available and the projection nature of the images. The formation of O_2 molecules has been suggested to be due to TM oxidation, TM-layer Li deintercalation, in-plane TM migration, and the resulting vacancy clusters.[11] In such processes, the out-of-plane O–O(2M) and O–O(M) are seen to be mostly affected, displaying contraction compared with the relative stable in-plane O–O(MLi) distance. The smaller magnitude of the change in O–O(2M) is possibly due to the out-of-plane TM migration to the alkali layer that is not considered in the DFT calculations. Such migration, resulting in ~5%–6% occupancy of the alkali layer can draw the oxygen away from the cations in the TM layer.[25,31] The out-of-plane TM migration effect is a potential explanation for the smaller magnitude in the layer expansion than the DFT predicted, resulting from the shielding of TMs in the alkali layer that weakens oxygen repulsion. We note that although the DFT_O_2 model provides the closest agreement to our experimental results, some of the shifts measured remain smaller than the model, which may be explained by oxygen release in the near surface region compensating some of the charge transfer needed during the initial charging.[32,33]

On discharge of $Li_{1.2}[Ni_{0.13}Mn_{0.54}Co_{0.13}]O_2$, the layer expansion of M–M(OLiO) is seen to recover, and O-O(Li) layers partially recover, presumably as a result of the reintercalation of the alkali layers, see Figure 3M. The distortions of the [TMO_6] octahedra are seen not to recover, however, and possibly contract further, Figure 3N. The irreversible oxygen shifts after the first cycle can explain and coincide with the findings from bulk-sensitive X-ray absorption spectroscopy (XAS) studies where the shape of the XAS lines of TMs, indicating [TMO_6] octahedral distortion and first-shell bond lengths, differs from the pristine state.[34–37] Multiple reported reasons may account for the irreversible oxygen shift. First, the reintercalated Li^+ ions occupy the vacancies left by in-plane TM migration during charging, resulting in an increasing amount of O^{2-} ions only coordinated with Li^+ ions (O-Li_6), different from the pristine structure where each O^{2-} ion is bonded with two TMs and four Li^+ ions (O-Li_4Mn_2).[11] Second, the out-of-plane TM migration in the bulk is only partially reversible.[4] Third, the TMs after discharge may contain a growing number of Jahn-Teller active ions compared with that in the pristine structure, such as the Mn^{3+} ions[9,10] and Ni^{3+} ions[22] that have been probed by the bulk-sensitive transmission or fluorescence mode XAS. In our DFT calculations on the discharged model, only the first factor is considered, whereas the latter two are not, potentially leading

Table 2. Changes of the projected distance of $Li_{1.2}[Ni_{0.13}Mn_{0.54}Co_{0.13}]O_2$ from the pristine to oxidized state

Bulk region		Experimental	DFT_O_2	DFT_V_{O2}	DFT_hole	DFT_TM
TMO_6	O–O(M)	−3.2%	−3.1%	−5.7%	−5.7%	−8.7%
	O–O(MLi)	0	0.6%	−0.5%	−1.0%	−0.5%
	O–O(2M)	−3.3%	−6.5%	−9.9%	−8.3%	−5.0%
Layers	M–M(OLiO)	1.7%	2.7%	1.4%	2.8%	−3.0%
	O–O(Li)	5.1%	7.7%	7.6%	10.3%	1.9%
Ratio of O-O(Li)/M-M(OLiO)		2.95	2.91	5.5	3.64	−0.64

Results are presented from experimental measurements and DFT modeling of four oxidized models of $Li_{1.2}[Ni_{0.13}Mn_{0.54}Co_{0.13}]O_2$ in charging. DFT_O_2 models O_2 molecules trapped in vacancy clusters, DFT_V_{O2} models the trapped O_2 molecules removed from the vacancies, DFT_hole models the formation of electron holes, and DFT_TM models pure cation oxidation.

to the DFT results (Table S4) deviating from the experimental measurements on the discharged structure.

In summary, in the first cycle of $Li_{1.2}[Ni_{0.13}Mn_{0.54}Co_{0.13}]O_2$, the bulk oxygen shifts from the original positions of pristine state and forms highly contracted [TMO_6] octahedra. The distorted oxygen sublattice in charging cannot recover in discharging, accounting for the first-cycle voltage hysteresis. The unrecovered oxygen shift and octahedral distortion result in both the TM and O environment being different from the pristine sate. This leads to altered voltage profiles of $Li_{1.2}[Ni_{0.13}Mn_{0.54}Co_{0.13}]O_2$ in sequential charging with decreased voltage plateaus of both cationic and oxygen oxidation (see Figure S4).

Surface layer reconstruction

Figures 4A and 4B show the simultaneous HAADF and ptychographic image of the surface region of pristine $Li_{1.2}[Ni_{0.13}Mn_{0.54}Co_{0.13}]O_2$, respectively, both at a dose of 8.1×10^4 $e^-/Å^2$. The lack of contrast from alkali layers in the HAADF image, consistent with Figure 3A, suggests that cation mixing is invisible in the pristine sample. The ptychographic image reveals the same *ccp* oxygen sublattice as in the bulk. After charging and discharging of $Li_{1.2}[Ni_{0.13}Mn_{0.54}Co_{0.13}]O_2$, the respective HAADF images in Figures 4C and 4E exhibit reconstructed cubic structures over the surface resulting from the out-of-plane TM migration and cation mixing in the alkali layers, consistent with the multiframe ADF imaging in Figures 3D and 3G. Out-of-plane TM migration has been reported to be driven by the oxygen loss that results in an unstable [TMO_5] structure at the surface.[26] The reformed cubic structures are Li-poor spinel-like and disordered rocksalt, depending on whether the cations alternatively occupy the Li sites or occupy all the Li sites randomly. The spinel-like structure has been proposed with several models (Figure S20), such as $LiMn_2O_4$-type,[38] Mn_3O_4-type,[39] and low-temperature (LT) $LiCoO_2$-type,[27] according to whether the tetrahedral sites are occupied. Electron ptychography can directly image the tetrahedral sites and identify the spinel model. Figures 4D and 4F show the ptychographic images of charged and discharged $Li_{1.2}[Ni_{0.13}Mn_{0.54}Co_{0.13}]O_2$, respectively, showing that most of the tetrahedral sites in the structures lack high contrast, and the formed spinel-like structure is mostly a LT $LiCoO_2$-type phase[27] with *ccp*-oxygen packing.

Oxygen shift in reconstructed surface layers

In measuring the atom distance at the surface, we carried out the same protocol as used for the bulk. Figures S21–S26 show the ptychographic images of the samples at different stages of the cycling, and Tables S8–S10 are the full list of the distances. Table 3 and Figure 4G display the atom distances in the surface region, and their variations, depicted by the displacement vectors, are plotted in Figures 4H–4K. In the

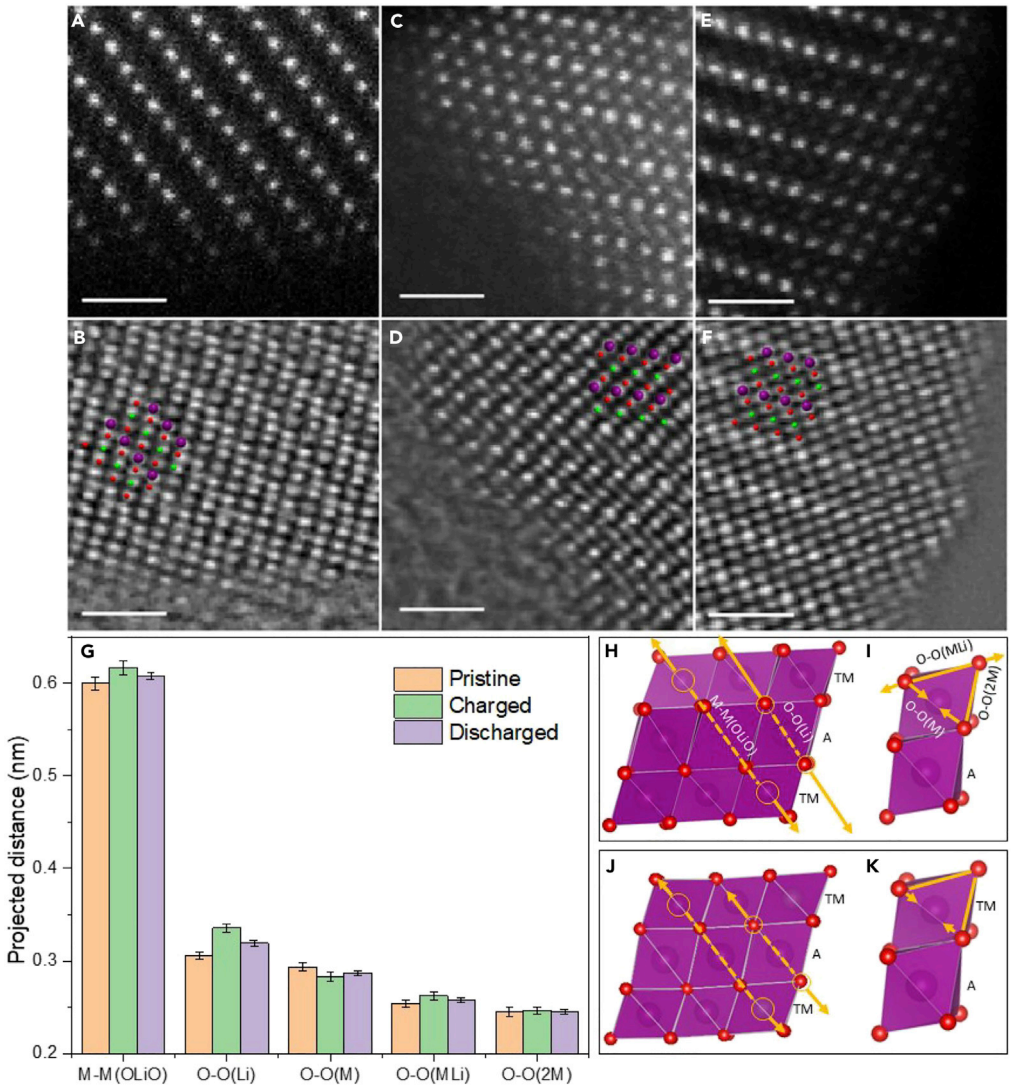

Figure 4. Simultaneous HAADF and WDD phase images of the surface region along the $[010]_{monoclinic}$ projection of $Li_{1.2}[Ni_{0.13}Mn_{0.54}Co_{0.13}]O_2$

(A–F) (A, C, and E) HAADF image. (B, D, and F) WDD phase image. (A and B) Pristine state with a dose of 8.1×10^4 $e^-/Å^2$. (C and D) Charged state with a dose of 4.3×10^4 $e^-/Å^2$. (E and F) Discharged state with a dose of 8.3×10^4 $e^-/Å^2$. Superimposed in (B, D, and F) is the atomic model where purple is TM, red is oxygen, and green is Li. Scale bar in all images is 1 nm.

(G–K) (G) Bar chart of the measured atom distances. M-M(OLiO) and O-O(Li) indicate the layer spacing and the right three O–O distances represent [TMO_6] octahedra. Schematic displacement vectors of the (H and J) layer spacing and (I and K) [TMO_6] octahedra at (H and I) charged and (J and K) discharged states compared with pristine state. Purple octahedra represent [TMO_6]. TM layers and alkali layers are indicated by TM and A in (H–K), respectively. The TMs in the alkali layers represent cation mixing formed by out-of-plane TM migration. In [TMO_6], the equatorial and axial O–O direction is the same as illustrated in Figure 3.

schematic structures, the alkali layers of the surface region are mostly occupied by the out-plane migrated TMs with a preference to be Ni ions.[40]

In charging, M–M(OLiO) increases by 2.8% and O–O(Li) by 10% across the layers indicating the layer expansion, consistent with the change in the bulk. The magnitudes in the fractional change of both O–O(Li) and M–M(OLiO) and the changing ratio of O–O(Li)/M–M(OLiO) are larger than that in the bulk. However, O–O(Li) may be expected to have a smaller fractional increase than the bulk because it has been suggested that the electrostatic repulsion of oxygen layers can be shielded by the

Table 3. Mean atom distances of $Li_{1.2}[Ni_{0.13}Mn_{0.54}Co_{0.13}]O_2$ from a surface region after drift calibration

Surface region		Pristine	Charged	Δ(Charge-pristine)	Discharged	Δ(Discharge-pristine)
TMO_6	O-O(M)	0.294 ± 0.004	0.283 ± 0.005	−3.5%	0.287 ± 0.003	−2.1%
	O-O(MLi)	0.254 ± 0.004	0.262 ± 0.004	3.3%	0.258 ± 0.003	1.3%
	O-O(2M)	0.245 ± 0.004	0.247 ± 0.004	0.6%	0.246 ± 0.002	0.1%
Layers	M-M(OLiO)	0.600 ± 0.007	0.617 ± 0.007	2.8%	0.608 ± 0.004	1.4%
	O-O(Li)	0.305 ± 0.004	0.336 ± 0.007	10.0%	0.320 ± 0.003	4.7%

The results are measured from pristine, first-charged and first-discharged states. Unit is nm. The difference of charged and discharged sample is relative to the pristine.

alkali-layer ions.[41] In standard cubic rocksalts (Fm-3m) and LT $LiCoO_2$-type spinels (Fd-3m), the projected length ratio of O–O(Li)/M–M(OLiO) is 0.5–0.52, smaller than that measured from the charged surface, 0.55. The results indicate that the reformed cubic structures at the surface are not the same as the standard cubic structure and have lattice distortions when evolved from the pristine layered structure, as previously suggested.[38,42]

In the $[TMO_6]$ octahedra, O–O(M) contracts by 3.5%, similar to the bulk region. However, the expansion of O–O(MLi) by 3.3% and almost stable O–O(2M) are different, implying the octahedral distortion of $[TMO_6]$ at the surface is different from that in the bulk. In the bulk, the octahedral distortions were most consistent with the DFT predictions for a model containing trapped O_2 molecules formed during charging, and the difference may be associated with the lack of O_2 molecules as they are lost at the surface. The case is mostly the irreversible oxygen loss in the format of free O_2 and CO_2 molecules and oxygen-containing deposits.[3,25] The oxygen loss generates unstable $[TMO_5]$ structures, driving the out-of-plane TM migration and formation of cubic phase and densification at surface.[26] In such a process, the electronic structure and the local environment of TMs and O have been hugely altered.[9] The expansion of O–O(MLi) suggests the resulting distortion of the oxygen sublattice unlike that in the bulk. We cannot rule out the impact of Jahn-Teller distortion resulting from the Mn^{3+} ions reduced from Mn^{4+} ions during the oxygen loss at high charging voltages[36] and the Ni^{3+} ions left by incomplete oxidation.[36] In charging, the $[TMO_6]$ octahedra are stretched along the axial O–O direction (Figure 4I); such distortion, unlike that in the bulk, indicates complicated surface structural changes in oxidation with a low probability of forming reversible O_2 molecules in the surface lattice.

In discharging, M–M(OLiO) recovers to pristine distance within the measurement error. Recovery of the $[TMO_6]$ octahedral distortions toward the pristine configuration is also seen, although close to the measurement error. Such surface oxygen sublattice recovered with residues, unlike the bulk, may be unexpected since TM migration and oxygen loss at the surface are observed. The cubic layers resulting from TM migration in charging are still seen after discharging. Oxygen loss can shift the Fermi level of the structure and allow the empty e_g states of Mn and Co to be available for Li reintercalation, resulting in over reduction of Mn^{4+}/Co^{3+} that leads to Jahn-Teller distortion of the $[TMO_6]$ octahedra.[9,25,35] After the first cycle, the formed oxygen sublattice at the surface is expected to be robust against oxygen evolution in the following cycles because of the absence of oxygen evolution from the second cycle of charging.[43]

Conclusions

We have shown that the oxygen sublattice deformation of $Li_{1.2}[Ni_{0.13}Mn_{0.54}Co_{0.13}]O_2$ in the first cycle can be directly imaged with sub-Angstrom precision

measurements of oxygen displacements. Distinct distortions in the bulk and surface regions are seen indicating different oxygen redox mechanisms in the two regions. To illustrate the use of the measurements, the [TMO_6] octahedral distortions in the bulk region on charging are compared with three models and found to be most consistent with DFT calculations assuming O_2 molecules are formed in the structure vacancies though with some significant discrepancies. The comparison presented here, although supportive of the model of the formation of trapped O_2 molecules, forms part of a wider body of evidence rather than being conclusive alone. The differences seen in the surface measurements may be associated with irreversible oxygen loss. The oxygen loss from the surface is associated with the cation mixing and cubic structure reformation. After discharging, the [TMO_6] octahedra in the bulk remain distorted from the pristine situation, potentially resulting from the irreversible oxygen displacements following TM migration and possibly Jahn-Teller distortion associated with the TM ions. However, the octahedra at the surface recover toward the pristine configurations with some residues, despite oxygen loss and cation mixing. The bulk oxygen shift in charging but unrecovered in discharging is expected to account for the voltage hysteresis seen in $Li_{1.2}[Ni_{0.13}Mn_{0.54}Co_{0.13}]O_2$. The nearly recovered [$TMO_6$] octahedral distortions at the surface after discharging potentially result from the coincidental opposite effects of Jahn-Teller distortion and oxygen shift in the cubic structure reconstruction. After the first cycle, the altered oxygen sublattice primarily occurring in the bulk, together with the changed surface structure result in different coordination environment of TMs and Li ions from that in the pristine and distinct voltage profiles in following cycles.

The oxygen shifts seen in both the bulk and surface regions are highly indicative of the respective TM migration and oxygen redox processes, which are crucial to the building of comprehensive understandings on oxygen redox. To improve the reversibility of oxygen distortion, developing superstructures suppressing metal migration and surface manipulation against oxygen loss are essential. In this work, we evidence that electron ptychography offers new opportunities to precisely interpret the atomic structure and measure the projected atom bonds of battery materials, unveiling the shift of both heavy and light atoms during electrochemical reaction. Such local, high-resolution structural information aids the development of the understandings of these materials in terms of the redox mechanism.

EXPERIMENTAL PROCEDURES

Resource availability

Lead contact

Further information and requests for resources should be directed to and will be fulfilled by the lead contact, Peter D. Nellist (peter.nellist@materials.ox.ac.uk).

Materials availability

This study did not generate new unique reagents.

Data and code availability

The data and codes used in this study are available from the corresponding authors on reasonable request.

Material synthesis

For the synthesis of $Li_{1.2}Mn_{0.54}Co_{0.13}Ni_{0.13}O_2$ a resorcinol-formaldehyde sol-gel method was used. Stoichiometric amounts of $LiCH_3COO{\cdot}2H_2O$ (99.0%, Aldrich), $Co(CH_3COO)_2{\cdot}4H_2O$ (99.0%, Aldrich), $Ni(CH_3COO)_2{\cdot}4H_2O$ (99.0%, Aldrich), and $Mn(CH_3COO)_2{\cdot}4H2O$ (99.0%, Fluka) were dissolved in 50 mL of distilled water. A

separate mixture containing 0.1 mol of resorcinol (99.0%, Fluka), 0.15 mol of formaldehyde (Fluka 36.5% in water, methanol-stabilized), and 0.25 mmol of Li_2CO_3 (99.0%, Fluka) was also made. Both solutions were stirred until all the reagents had dissolved, before being added together and stirred for 30 min. Note that a 5 mol % excess of Li was used. The mixture was then dried at 90°C for 8 h, followed by a burning of the organic matter at 480°C for 15 h. The fine powder was removed from the furnace, ground down, and calcined at 900°C for 15 h to obtain the final material.

Electrochemical characterization

The cathode was prepared by mixing 80 wt % active material, 10 wt % Super P conductive carbon, and 10 wt % polytetrafluoroethylene binder in a mortar and rolling into a film. CR2032 coin cells were assembled using the prepared cathode, glass fiber separators, 1 M $LiPF_6$ in EC/DMC (v/v = 1:1) as the electrolyte and lithium foil as the anode. The current density used was 10 mA g^{-1}, with a voltage window of 2 to 4.8 V being used for cycling.

Specimen preparation and TEM transfer

After either fully charging or discharging of $Li_{1.2}[Ni_{0.13}Mn_{0.54}Co_{0.13}]O_2$, the cathode material was collected from the cells and washed with DMC solvent in the glovebox, following by grinding and sonication. The solution dispersion was dropped on the TEM grids followed by drying in the glovebox at room temperature. The TEM grids were mounted on the JEOL air-free transfer TEM holder in the glovebox following by transfer to the microscope for imaging.

ADF and 4D-STEM data collection

The electron microscopy study was carried out on an aberration-corrected JEOL ARM200F electron microscope operated at 200 kV. In ADF STEM imaging, the convergence semiangle was 22.4 mrad and the inner and outer collection angles were 72.8–271 mrad. Multiframe ADF imaging was carried out through SmartAlign to minimize the dose to the sample and scan distortions. A total number of eight frames were collected from a same field of view. Each frame is in 512 × 512 pixels at a dwell time of 1–8 μs. The sequence of images were aligned and averaged using rigid registration algorithm followed by nonrigid registration.

In the 4D STEM dataset recording, a focused STEM probe was used and the 2D CBED pattern at each probe position were recorded using a JEOL 4Dcanvas pixelated detector mounted on ARM200F. The camera has 264 × 264 physical pixels and through pixel binning by 4-fold (64 × 264 pixels), the recording speed can reach ~7.5k frames per second, which is the speed used in this work of all the 4D datasets. The real-space 2D raster scanning contains 256 × 256 pixels, resulting in the recording of 256 × 256 frames of diffraction patterns in ~8.7 s. The emission current of the electron gun is down to 6 μA or below from the original 15 μA to avoid the saturation of the pixelated detector while lowering the beam damage. The used probe current is below 11.4 pA. The dose of each datasets may depend on the real-time probe current and pixel size and is shown in the figure caption of its corresponding image. The aberration-corrected ADF images were recorded simultaneously using the JEOL ADF detector with the collection of 2D diffraction patterns.

Electron ptychography reconstruction

Ptychographic reconstruction of the phase image of the sample is a postprocessing of the entire CBEDs. Wigner distribution deconvolution algorithm is one of the commonly used method to retrieve the phase information. In reconstruction, the

residual aberrations in the datasets can be corrected by numerical processing. To do this, an optimized probe function was determined by measuring the aberrations through the singular value decomposition (SVD) algorithm and correcting them. Aberration-free phase images were then reconstructed. The particle samples generally have uneven thickness and cause large deviation in the defocus aberration over the whole field of view of the sample. The numerical processing by tuning the defocus value that calculated in optimizing probe function allows to form the phase image at specific defocus and to exhibit a well-focused phase image of a specific field of view. Detailed mathematics of the ptychographic reconstruction and aberration corrections were previously reported by our group, see Yang et al.,[13] Nellist et al.,[16] O'Leary et al.,[17] Pennycook et al.,[18] Yang et al.,[19] and Pennycook et al.,[21]

Density functional theory (DFT)

Spin-polarized calculations were carried out using the Quantum Espresso suite,[44] using the Perdew, Burke, and Ernzerhof (PBE) exchange-correlation functional.[45] The core-valence interaction was described via norm-conserving pseudopotentials.[46] The wavefunctions were represented via plane-wave basis sets with an energy cutoff of 120 Ry. Hubbard corrections (DFT + U) were included to correctly describe the energetics of the *3d* orbitals of the TM, with U = 4, 6, and 5 eV for Mn, Ni, and Co, respectively. A 2 × 2 × 4 Monkhorst–Pack k-point grid was used. Crystal structures were relaxed until forces on the atoms were less than 0.02 eV/Angstrom, and total stresses on the cell were less than 0.05 kBar. On top of the DFT + U simulations, we performed hybrid calculations employing the Heyd–Scuseria–Ernzerhof (HSE) functional,[44] with an exact exchange mixing parameter of 0.25. The input structures were obtained from the DFT + U optimizations, and the atomic positions were allowed to further relax at the HSE level, keeping the lattice parameters fixed. A correction of 1.06 eV/O_2 was introduced to calculate formation energies, in order to remediate the overestimation of the binding energy of O_2 by the HSE functional.[47,48] A supercell containing 96 atoms (28 Li atoms, 12 Mn atoms, 4 Ni atoms, 4 Co atoms, and 48 O atoms) was optimized and used as initial structure to investigate charged and discharged states. To study in-plane TM disorder in the charge state, structural models with different TM distributions in the TM layers were prepared using combinatorics. Simple random sampling (SRS) was used to choose a representative subset of configurations for relaxation. The optimized structures with the lowest formation energies for the pristine, charged and discharged states are shown in Figure S18. Projected atom distances were computed on these models.

SUPPLEMENTAL INFORMATION

Supplemental information can be found online at https://doi.org/10.1016/j.joule.2022.04.008.

ACKNOWLEDGMENTS

Support is gratefully acknowledged from the EPSRC (EP/K040375/1 "South of England Analytical Electron Microscope"), the Henry Royce Institute for Advanced Materials (EP/R00661X/1, EP/S019367/1, and EP/R010145/1), and the Faraday Institution (FIRG007, FIRG008, and FIRG016). We acknowledge the David Cockayne Centre for Electron Microscopy at the University of Oxford and electron Physical Sciences Imaging Centre (no. MG22479) at the Diamond Light Source, UK, for access and support. We acknowledge the resources provided by the Cambridge Tier-2 system operated by the University of Cambridge Research Computing

Service (http://www.hpc.cam.ac.uk) funded by EPSRC Tier-2 capital grant EP/P020259/1, via the BATTSurface and BATTDesign projects.

AUTHOR CONTRIBUTIONS

W.S. and P.D.N. conceived the work. W.S. prepared TEM samples and collected and processed the electron microscopy datasets. M.A.P.-O. performed the DFT calculations. J.J.M. synthesized the sample and carried out testing. E.L. and X.L. helped on imaging simulation. C.O.L. helped on electron ptychography reconstruction. W.S., M.A.P.-O., J.J.M., R.A.H., P.G.B., and P.D.N. discussed the data and interpretation. W.S. and P.D.N. wrote the manuscript, with contributions and comments from all authors.

DECLARATION OF INTERESTS

The authors declare no competing interests.

Received: November 21, 2021
Revised: February 23, 2022
Accepted: April 11, 2022
Published: May 6, 2022

REFERENCES

1. Assat, G., and Tarascon, J.-M. (2018). Fundamental understanding and practical challenges of anionic redox activity in Li-ion batteries. Nat. Energy *3*, 373–386.

2. Noh, H.-J., Youn, S., Yoon, C.S., and Sun, Y.-K. (2013). Comparison of the structural and electrochemical properties of layered Li $[Ni_xCo_yMn_z]O_2$ (x = 1/3, 0.5, 0.6, 0.7, 0.8 and 0.85) cathode material for lithium-ion batteries. J. Power Sources *233*, 121–130.

3. Luo, K., Roberts, M.R., Hao, R., Guerrini, N., Pickup, D.M., Liu, Y.-S., Edström, K., Guo, J., Chadwick, A.V., Duda, L.C., and Bruce, P.G. (2016). Charge-compensation in 3d-transition-metal-oxide intercalation cathodes through the generation of localized electron holes on oxygen. Nat. Chem. *8*, 684–691.

4. Gent, W.E., Lim, K., Liang, Y., Li, Q., Barnes, T., Ahn, S.J., Stone, K.H., McIntire, M., Hong, J., Song, J.H., et al. (2017). Coupling between oxygen redox and cation migration explains unusual electrochemistry in lithium-rich layered oxides. Nat. Commun. *8*, 2091.

5. Croy, J.R., Balasubramanian, M., Gallagher, K.G., and Burrell, A.K. (2015). Review of the U.S. Department of Energy's "deep dive" effort to understand voltage fade in Li- and Mn-rich cathodes. Acc. Chem. Res. *48*, 2813–2821.

6. Assat, G., Foix, D., Delacourt, C., Iadecola, A., Dedryvère, R., and Tarascon, J.-M. (2017). Fundamental interplay between anionic/cationic redox governing the kinetics and thermodynamics of lithium-rich cathodes. Nat. Commun. *8*, 2219.

7. Assat, G., Delacourt, C., Corte, D.A.D., and Tarascon, J.-M. (2016). Editors' choice—practical assessment of anionic redox in Li-rich layered oxide cathodes: a mixed blessing for high energy Li-ion batteries. J. Electrochem. Soc. *163*, A2965–A2976.

8. Eum, D., Kim, B., Kim, S.J., Park, H., Wu, J., Cho, S.P., Yoon, G., Lee, M.H., Jung, S.K., Yang, W., et al. (2020). Voltage decay and redox asymmetry mitigation by reversible cation migration in lithium-rich layered oxide electrodes. Nat. Mater. *19*, 419–427.

9. Hu, E., Yu, X., Lin, R., Bi, X., Lu, J., Bak, S., Nam, K.-W., Xin, H.L., Jaye, C., Fischer, D.A., et al. (2018). Evolution of redox couples in Li- and Mn-rich cathode materials and mitigation of voltage fade by reducing oxygen release. Nat. Energy *3*, 690–698.

10. House, R.A., Maitra, U., Pérez-Osorio, M.A., Lozano, J.G., Jin, L., Somerville, J.W., Duda, L.C., Nag, A., Walters, A., Zhou, K.J., et al. (2020). Superstructure control of first-cycle voltage hysteresis in oxygen-redox cathodes. Nature *577*, 502–508.

11. House, R.A., Rees, G.J., Pérez-Osorio, M.A., Marie, J.-J., Boivin, E., Robertson, A.W., Nag, A., Garcia-Fernandez, M., Zhou, K.-J., and Bruce, P.G. (2020). First-cycle voltage hysteresis in Li-rich 3d cathodes associated with molecular O_2 trapped in the bulk. Nat. Energy *5*, 777–785.

12. Sathiya, M., Leriche, J.B., Salager, E., Gourier, D., Tarascon, J.M., and Vezin, H. (2015). Electron paramagnetic resonance imaging for real-time monitoring of Li-ion batteries. Nat. Commun. *6*, 6276.

13. Yang, H., MacLaren, I., Jones, L., Martinez, G.T., Simson, M., Huth, M., Ryll, H., Soltau, H., Sagawa, R., Kondo, Y., et al. (2017). Electron ptychographic phase imaging of light elements in crystalline materials using Wigner distribution deconvolution. Ultramicroscopy *180*, 173–179.

14. Liberti, E., Lozano, J.G., Pérez Osorio, M.A., Roberts, M.R., Bruce, P.G., and Kirkland, A.I. (2019). Quantifying oxygen distortions in lithium-rich transition-metal-oxide cathodes using ABF STEM. Ultramicroscopy *210*, 112914.

15. Shibata, N., Findlay, S.D., Kohno, Y., Sawada, H., Kondo, Y., and Ikuhara, Y. (2012). Differential phase-contrast microscopy at atomic resolution. Nat. Phys. *8*, 611–615.

16. Nellist, P.D., McCallum, B.C., and Rodenburg, J.M. (1995). Resolution beyond the "information limit" in transmission electron microscopy. Nature *374*, 630–632.

17. O'Leary, C.M., Martinez, G.T., Liberti, E., Humphry, M.J., Kirkland, A.I., and Nellist, P.D. (2021). Contrast transfer and noise considerations in focused-probe electron ptychography. Ultramicroscopy *221*, 113189.

18. Pennycook, T.J., Lupini, A.R., Yang, H., Murfitt, M.F., Jones, L., and Nellist, P.D. (2015). Efficient phase contrast imaging in STEM using a pixelated detector. Part 1: experimental demonstration at atomic resolution. Ultramicroscopy *151*, 160–167.

19. Yang, H., Pennycook, T.J., and Nellist, P.D. (2015). Efficient phase contrast imaging in STEM using a pixelated detector. Part II: optimisation of imaging conditions. Ultramicroscopy *151*, 232–239.

20. Lobato, I., Van Aert, S., and Verbeeck, J. (2016). Progress and new advances in simulating electron microscopy datasets using MULTEM. Ultramicroscopy *168*, 17–27.

21. Pennycook, T.J., Martinez, G.T., Nellist, P.D., and Meyer, J.C. (2019). High dose efficiency atomic resolution imaging via electron ptychography. Ultramicroscopy *196*, 131–135.

22. De Backer, A., van den Bos, K.H.W., Van den Broek, W., Sijbers, J., and Van Aert, S. (2016). StatSTEM: an efficient approach for accurate and precise model-based quantification of atomic resolution electron microscopy images. Ultramicroscopy *171*, 104–116.

23. Jones, L., Yang, H., Pennycook, T.J., Marshall, M.S.J., Van Aert, S., Browning, N.D., Castell, M.R., and Nellist, P.D. (2015). Smart Align—a new tool for robust non-rigid registration of scanning microscope data. Adv. Struct. Chem. Imaging *1*, 8.

24. Jones, L., Varambhia, A., Beanland, R., Kepaptsoglou, D., Griffiths, I., Ishizuka, A., Azough, F., Freer, R., Ishizuka, K., Cherns, D., et al. (2018). Managing dose-, damage- and data-rates in multi-frame spectrum-imaging. Microscopy (Oxf) *67*, i98–i113.

25. Yabuuchi, N., Yoshii, K., Myung, S.-T., Nakai, I., and Komaba, S. (2011). Detailed studies of a high-capacity electrode material for rechargeable batteries, Li_2MnO_3—$LiCo_{1/3}Ni_{1/3}Mn_{1/3}O_2$. J. Am. Chem. Soc. *133*, 4404–4419.

26. Koga, H., Croguennec, L., Ménétrier, M., Mannessiez, P., Weill, F., and Delmas, C. (2013). Different oxygen redox participation for bulk and surface: a possible global explanation for the cycling mechanism of $Li_{1.20}Mn_{0.54}Co_{0.13}Ni_{0.13}O_2$. J. Power Sources *236*, 250–258.

27. Zheng, J., Xu, P., Gu, M., Xiao, J., Browning, N.D., Yan, P., Wang, C., and Zhang, J.-G. (2015). Structural and chemical evolution of Li- and Mn-rich layered cathode material. Chem. Mater. *27*, 1381–1390.

28. Lu, P., Yan, P., Romero, E., Spoerke, E.D., Zhang, J.-G., and Wang, C.-M. (2015). Observation of electron-beam-induced phase evolution mimicking the effect of the charge–discharge cycle in Li-rich layered cathode materials used for Li ion batteries. Chem. Mater. *27*, 1375–1380.

29. Yang, H., Rutte, R.N., Jones, L., Simson, M., Sagawa, R., Ryll, H., Huth, M., Pennycook, T.J., Green, M.L.H., Soltau, H., et al. (2016). Simultaneous atomic-resolution electron ptychography and Z-contrast imaging of light and heavy elements in complex nanostructures. Nat. Commun. *7*, 12532.

30. Zhou, Y.N., Ma, J., Hu, E., Yu, X., Gu, L., Nam, K.W., Chen, L., Wang, Z., and Yang, X.Q. (2014). Tuning charge-discharge induced unit cell breathing in layer-structured cathode materials for lithium-ion batteries. Nat. Commun. *5*, 5381.

31. House, R.A., Marie, J.-J., Pérez-Osorio, M.A., Rees, G.J., Boivin, E., and Bruce, P.G. (2021). The role of O_2 in O-redox cathodes for Li-ion batteries. Nat. Energy *6*, 781–789.

32. Rana, J., Papp, J.K., Lebens-Higgins, Z., Zuba, M., Kaufman, L.A., Goel, A., Schmuch, R., Winter, M., Whittingham, M.S., Yang, W., et al. (2020). Quantifying the capacity contributions during activation of Li_2MnO_3. ACS Energy Lett. *5*, 634–641.

33. Guerrini, N., Jin, L., Lozano, J.G., Luo, K., Sobkowiak, A., Tsuruta, K., Massel, F., Duda, L.-C., Roberts, M.R., and Bruce, P.G. (2020). Charging mechanism of Li_2MnO_3. Chem. Mater. *32*, 3733–3740.

34. Koga, H., Croguennec, L., Ménétrier, M., Mannessiez, P., Weill, F., Delmas, C., and Belin, S. (2014). Operando X-ray absorption study of the redox processes involved upon cycling of the Li-rich layered oxide $Li_{1.2}Mn_{0.54}Co_{0.13}Ni_{0.13}O_2$ in Li ion batteries. J. Phys. Chem. C *118*, 5700–5709.

35. Ito, A., Sato, Y., Sanada, T., Hatano, M., Horie, H., and Ohsawa, Y. (2011). In situ X-ray absorption spectroscopic study of Li-rich layered cathode material $Li[Ni_{0.17}Li_{0.2}Co_{0.07}Mn_{0.56}]O_2$. J. Power Sources *196*, 6828–6834.

36. Oishi, M., Fujimoto, T., Takanashi, Y., Orikasa, Y., Kawamura, A., Ina, T., Yamashige, H., Takamatsu, D., Sato, K., Murayama, H., et al. (2013). Charge compensation mechanisms in $Li_{1.16}Ni_{0.15}Co_{0.19}Mn_{0.5}O_2$ positive electrode material for Li-ion batteries analyzed by a combination of hard and soft X-ray absorption near edge structure. J. Power Sources *222*, 45–51.

37. Oishi, M., Yogi, C., Watanabe, I., Ohta, T., Orikasa, Y., Uchimoto, Y., and Ogumi, Z. (2015). Direct observation of reversible charge compensation by oxygen ion in Li-rich manganese layered oxide positive electrode material, $Li_{1.16}Ni_{0.15}Co_{0.19}Mn_{0.5}O_2$. J. Power Sources *276*, 89–94.

38. Gu, M., Belharouak, I., Zheng, J., Wu, H., Xiao, J., Genc, A., Amine, K., Thevuthasan, S., Baer, D.R., Zhang, J.-G., et al. (2013). Formation of the spinel phase in the layered composite cathode used in Li-ion batteries. ACS Nano *7*, 760–767.

39. Yan, P., Nie, A., Zheng, J., Zhou, Y., Lu, D., Zhang, X., Xu, R., Belharouak, I., Zu, X., Xiao, J., et al. (2015). Evolution of lattice structure and chemical composition of the surface reconstruction layer in $Li_{1.2}Ni_{0.2}Mn_{0.6}O_2$ cathode material for lithium ion batteries. Nano Lett. *15*, 514–522.

40. Boulineau, A., Simonin, L., Colin, J.-F., Bourbon, C., and Patoux, S. (2013). First evidence of manganese–nickel segregation and densification upon cycling in Li-rich layered oxides for lithium batteries. Nano Lett. *13*, 3857–3863.

41. Laubach, S., Laubach, S., Schmidt, P.C., Ensling, D., Schmid, S., Jaegermann, W., Thissen, A., Nikolowski, K., and Ehrenberg, H. (2009). Changes in the crystal and electronic structure of $LiCoO_2$ and $LiNiO_2$ upon Li intercalation and de-intercalation. Phys. Chem. Chem. Phys. *11*, 3278–3289.

42. Ito, A., Shoda, K., Sato, Y., Hatano, M., Horie, H., and Ohsawa, Y. (2011). Direct observation of the partial formation of a framework structure for Li-rich layered cathode material $Li[Ni_{0.17}Li_{0.2}Co_{0.07}Mn_{0.56}]O_2$ upon the first charge and discharge. J. Power Sources *196*, 4785–4790.

43. Yin, W., Grimaud, A., Rousse, G., Abakumov, A.M., Senyshyn, A., Zhang, L., Trabesinger, S., Iadecola, A., Foix, D., Giaume, D., and Tarascon, J.-M. (2020). Structural evolution at the oxidative and reductive limits in the first electrochemical cycle of $Li_{1.2}Ni_{0.13}Mn_{0.54}Co_{0.13}O_2$. Nat. Commun. *11*, 1252.

44. Giannozzi, P., Baroni, S., Bonini, N., Calandra, M., Car, R., Cavazzoni, C., Ceresoli, D., Chiarotti, G.L., Cococcioni, M., Dabo, I., et al. (2009). QUANTUM ESPRESSO: a modular and open-source software project for quantum simulations of materials. J. Phys. Condens. Matter *21*, 395502.

45. Cococcioni, M., and de Gironcoli, S. (2005). Linear response approach to the calculation of the effective interaction parameters in the LDA + U method. Phys. Rev. B *71*, 035105.

46. Perdew, J.P., Burke, K., and Ernzerhof, M. (1996). Generalized gradient approximation made simple. Phys. Rev. Lett. *77*, 3865–3868.

47. Heyd, J., Scuseria, G.E., and Ernzerhof, M. (2003). Hybrid functionals based on a screened Coulomb potential. J. Chem. Phys. *118*, 8207–8215.

48. Kang, S., Mo, Y., Ong, S.P., and Ceder, G. (2013). A facile mechanism for recharging Li_2O_2 in Li–O_2 batteries. Chem. Mater. *25*, 3328–3336.

Joule, Volume *6*

Supplemental information

Direct imaging of oxygen shifts associated with the oxygen redox of Li-rich layered oxides

Weixin Song, Miguel A. Pérez-Osorio, John-Joseph Marie, Emanuela Liberti, Xiaonan Luo, Colum O'Leary, Robert A. House, Peter G. Bruce, and Peter D. Nellist

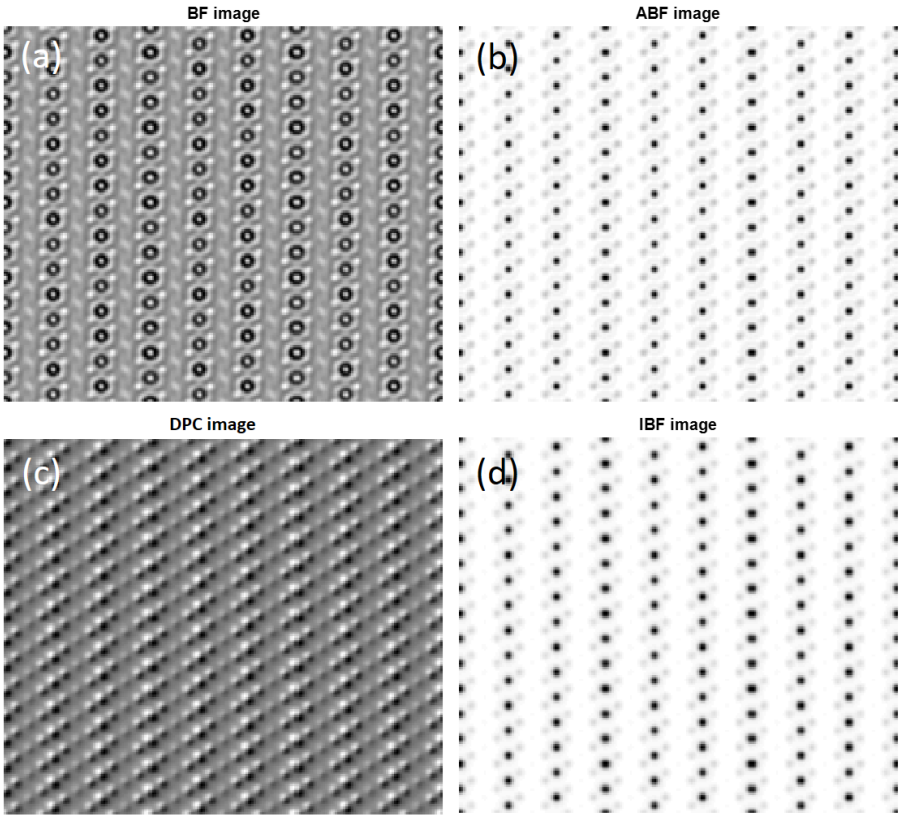

Figure S1. Synthetic images from the simulated 4D datasets of $Li_{1.2}[Ni_{0.13}Mn_{0.54}Co_{0.13}]O_2$. (a) BF image. (b) ABF image. (c) DPC image. (d) Incoherent BF image.

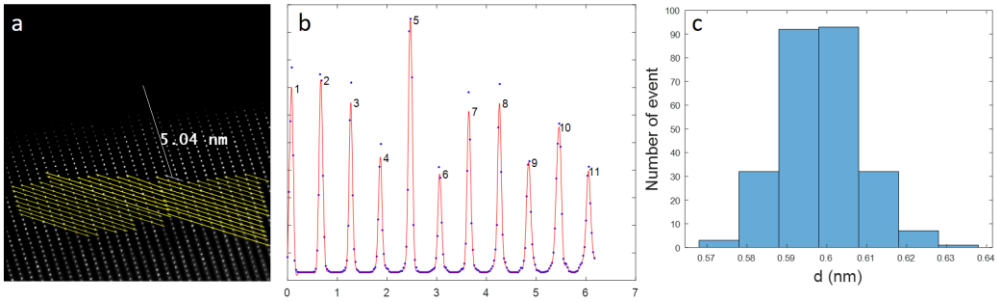

Figure S2. Atom distance measurement from drift-free ADF image.

(a) Zero-drift HAADF image of pristine Li-rich NMC generated from SmartAlign processing. (b) One of the line profiles from the yellow lines labelling the M-M(OLiO) orientation. The dots are the data point and red lines are fitted results using smoothspline program in MATLAB. (c) Histogram of the measured spacing.

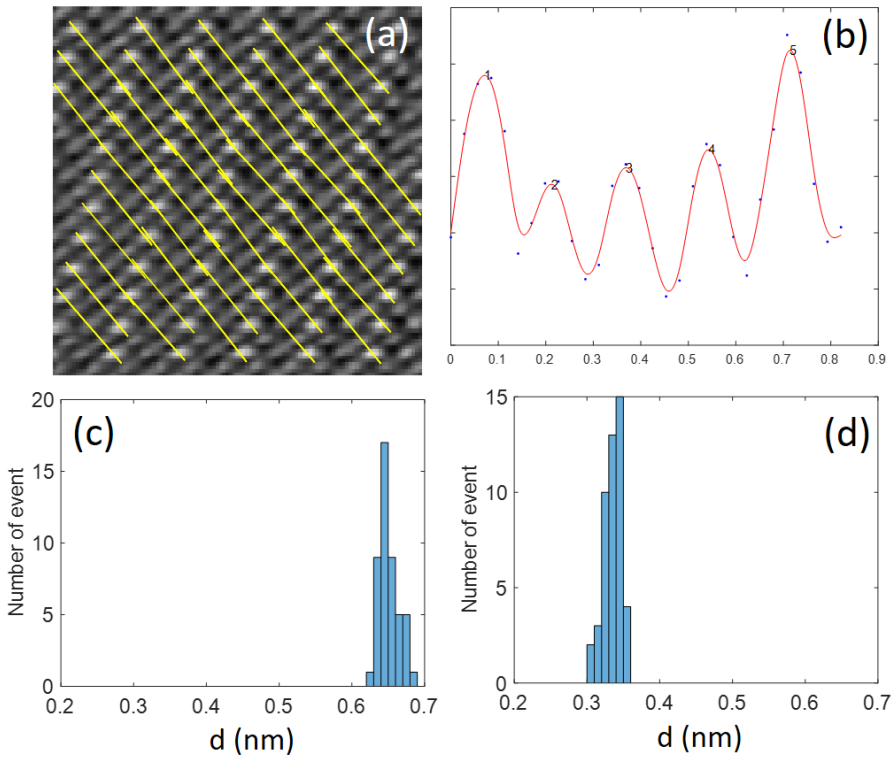

Figure S3. Atom distance measurement from ptychographic image.

(a) Ptychographic phase image of a bulk region of pristine Li-rich NMC. (b) One of the line profiles from the yellow lines labelling the M-M(OLiO) orientation. The dots are the data point and red lines are fitted results using smoothspline program in MATLAB. Histogram of the measured spacing of (c) M-M(OLiO) and (d) O-O(Li).

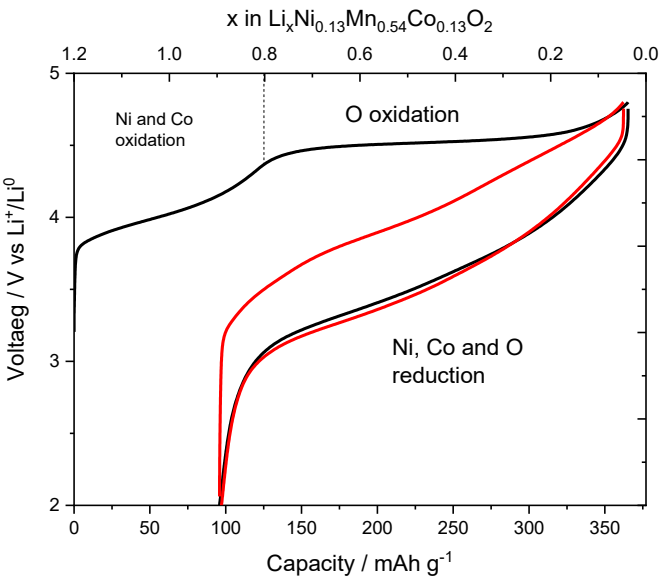

Figure S4. Galvanostatic charge-discharge profiles of $Li_{1.2}[Ni_{0.13}Mn_{0.54}Co_{0.13}]O_2$.
The current density is 10 mA/g and voltage is between 2 and 4.8 V vs. Li^+/Li. The first (black) and second (red) cycle exhibit changed voltage plateaus in charging.

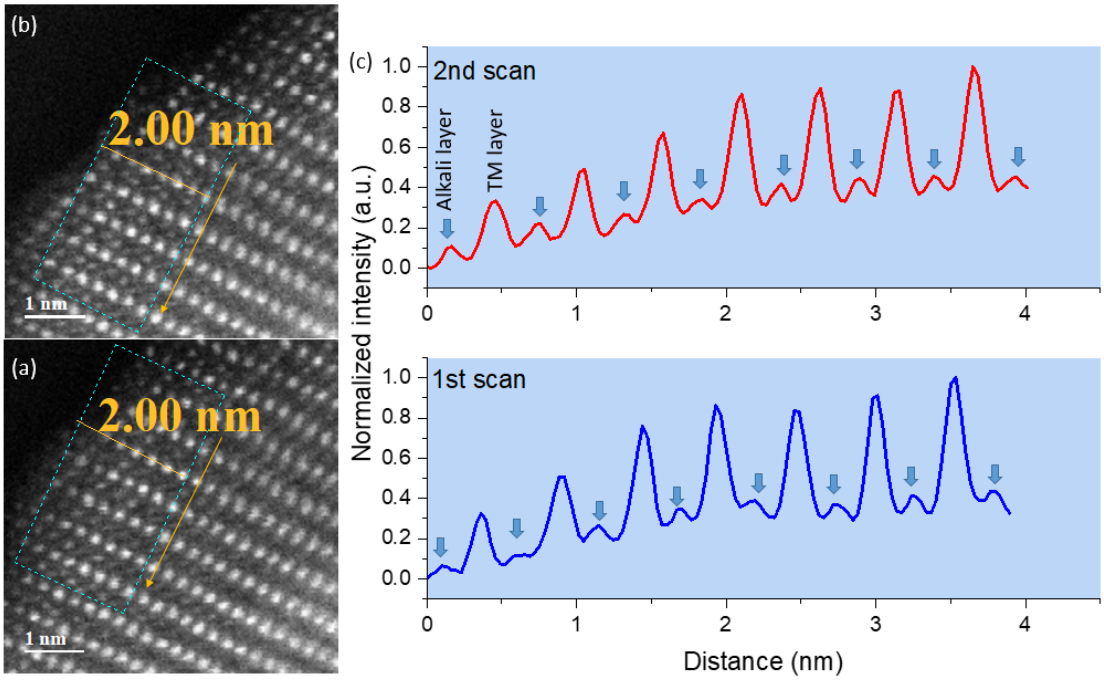

Figure S5. HAADF images of the charged $Li_{1.2}[Ni_{0.13}Mn_{0.54}Co_{0.13}]O_2$ collected in two sequential scans.

The electron dose is 8.1×10^4 $e^-/Å^2$. The accumulated dose of (a) the first frame is 8.1×10^4 $e^-/Å^2$ and (b) the second frame is 1.6×10^5 $e^-/Å^2$. The structures shown in the second-frame HAADF image are almost the same as the first one without further growing of the formed cubic layers. The line profiles averaged over a 2 nm thickness region in both frames are plotted in (c). The arrows labelled the contrast from alkali layers where cation mixing occurs. The ratios of the contrast from the alkali layers and adjacent TM layers are not seen heavily changed in the second frame relative to the first one, indicating such dose has not induced large beam damage to the sample.

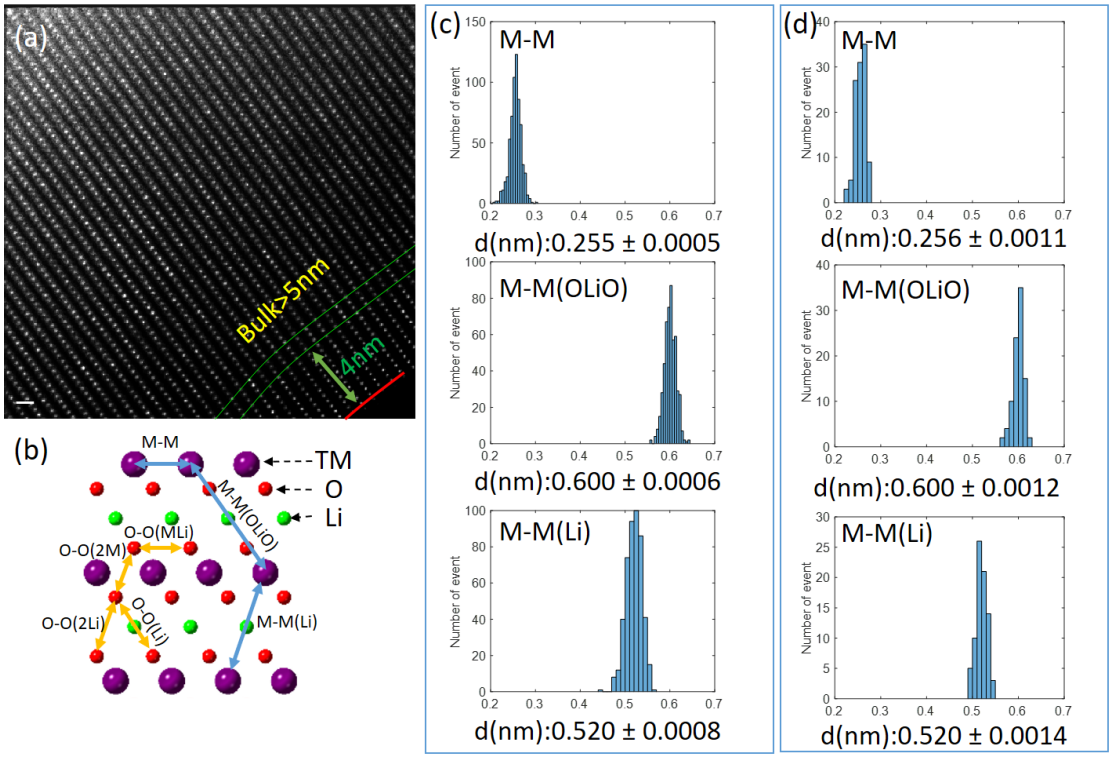

Figure S6. Statistics of the measurement of the three TM-TM distances, M-M, M-M(OLiO) and M-M(Li) from the bulk and surface region of pristine $Li_{1.2}[Ni_{0.13}Mn_{0.54}Co_{0.13}]O_2$.

The HAADF image in (a) is formed through rigid and non-rigid registration of 8 individual frames using SmartAlign program. The first ~4nm thickness region is the surface and beyond ~5nm is the bulk. Scale bar is 1 nm. (b) The crystal model showing the TM, O and Li atoms in the same projection as that in the HAADF image. Statistical results of the projected distances from (c) the bulk region and (d) the surface region.

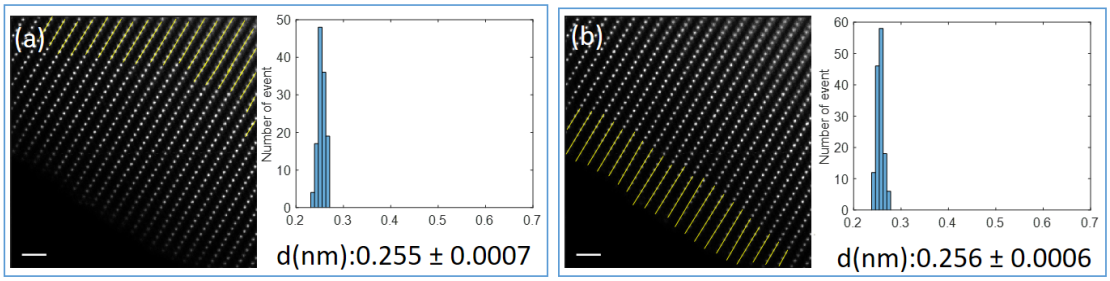

Figure S7. Statistics of the measurement of the M-M distance from a second particle of pristine $Li_{1.2}[Ni_{0.13}Mn_{0.54}Co_{0.13}]O_2$.

(a) Bulk region and (b) surface region. Scale bar is 1 nm. The HAADF image is collected using SmartAlign program from another particle to validate the data consistency and here only M-M distance is shown as an example.

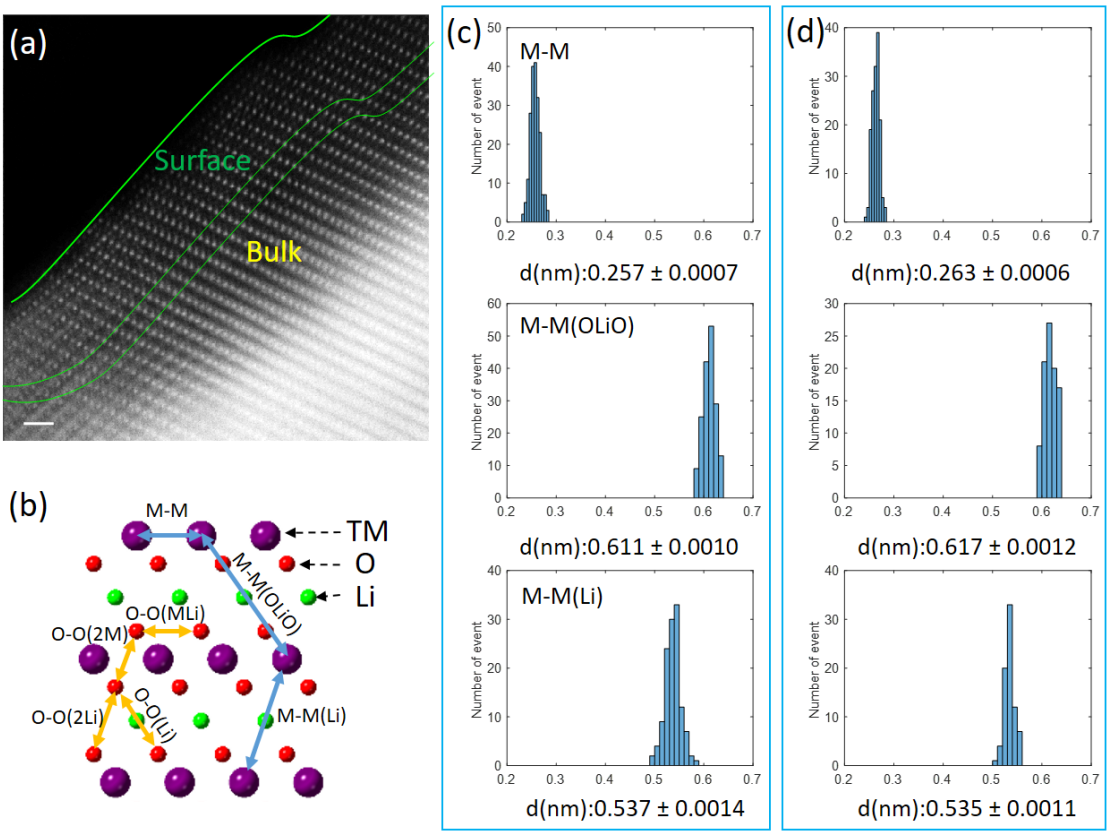

Figure S8. Statistics of the measurement of the three TM-TM distances, M-M, M-M(OLiO) and M-M(Li) from the bulk and surface region of charged $Li_{1.2}[Ni_{0.13}Mn_{0.54}Co_{0.13}]O_2$.

The HAADF image (a) is formed through rigid and non-rigid registration of 8 individual frames using SmartAlign program. The first ~4nm thickness region is the surface and beyond ~5nm is the bulk. Scale bar is 1 nm. (b) The crystal model showing the TM, O and Li atoms in the same projection as that in the HAADF image. Statistical results of the projected distances from (c) the bulk region and (d) the surface region.

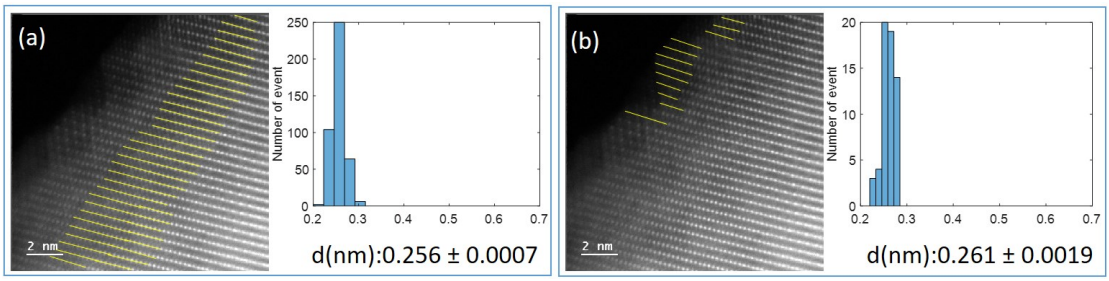

Figure S9. Statistics of the measurement of the M-M distance from a second particle of charged $Li_{1.2}[Ni_{0.13}Mn_{0.54}Co_{0.13}]O_2$.

(a) Bulk region and (b) surface region. The HAADF image is collected using SmartAlign program from another particle to validate the data consistency.

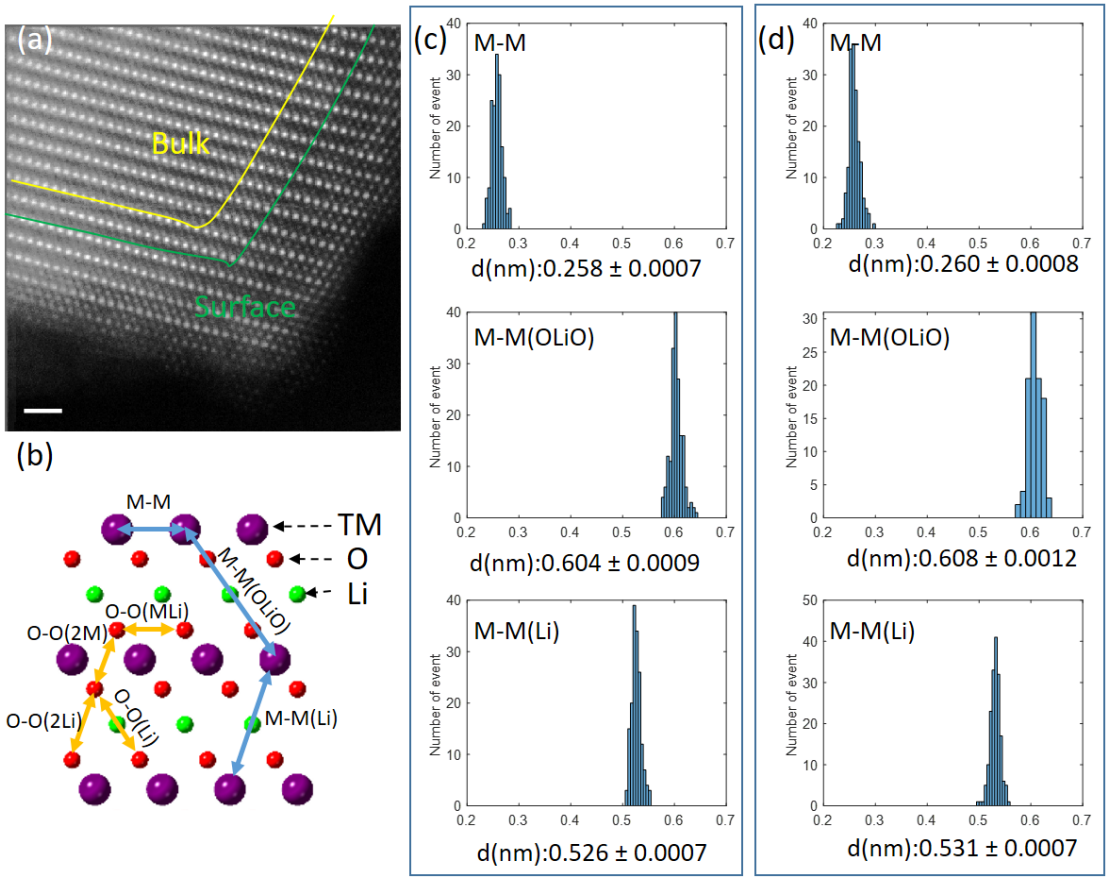

Figure S10. Statistics of the measurement of the three TM-TM distances, M-M, M-M(OLiO) and M-M(Li) from the bulk and surface region of discharged $Li_{1.2}[Ni_{0.13}Mn_{0.54}Co_{0.13}]O_2$.
The HAADF image (a) is formed through rigid and non-rigid registration of 8 individual frames using SmartAlign program. Scale bar is 1 nm. The first ~4nm thickness region is the surface and beyond ~5nm is the bulk. (b) The crystal model showing the TM, O and Li atoms in the same projection as that in the HAADF image. Statistical results of the projected distances from (c) the bulk region and (d) the surface region.

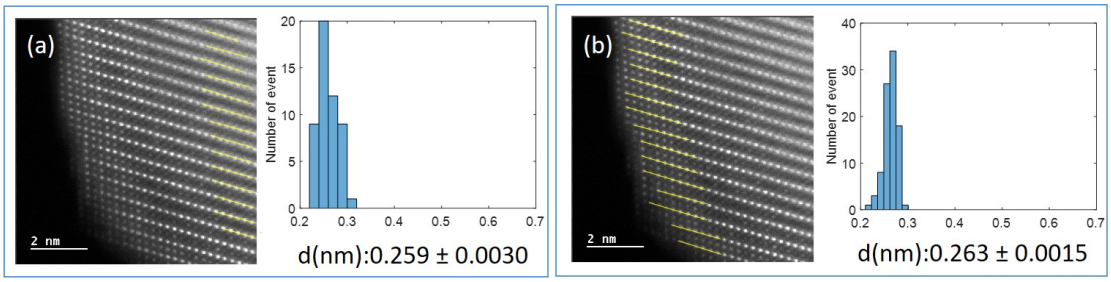

Figure S11. Statistics of the measurement of the M-M distance from a second particle of discharged $Li_{1.2}[Ni_{0.13}Mn_{0.54}Co_{0.13}]O_2$.

(a) Bulk region and (b) surface region. The HAADF image is collected using SmartAlign program from another particle to validate the data consistency. The little difference in the result of surface region from the first particle (0.2598 nm) may be from the complicated inhomogenous surface reaction in discharging. Nevertheless, the sub-angstrom accuracy of this measurement protocol indicates they are close to 0.26 nm.

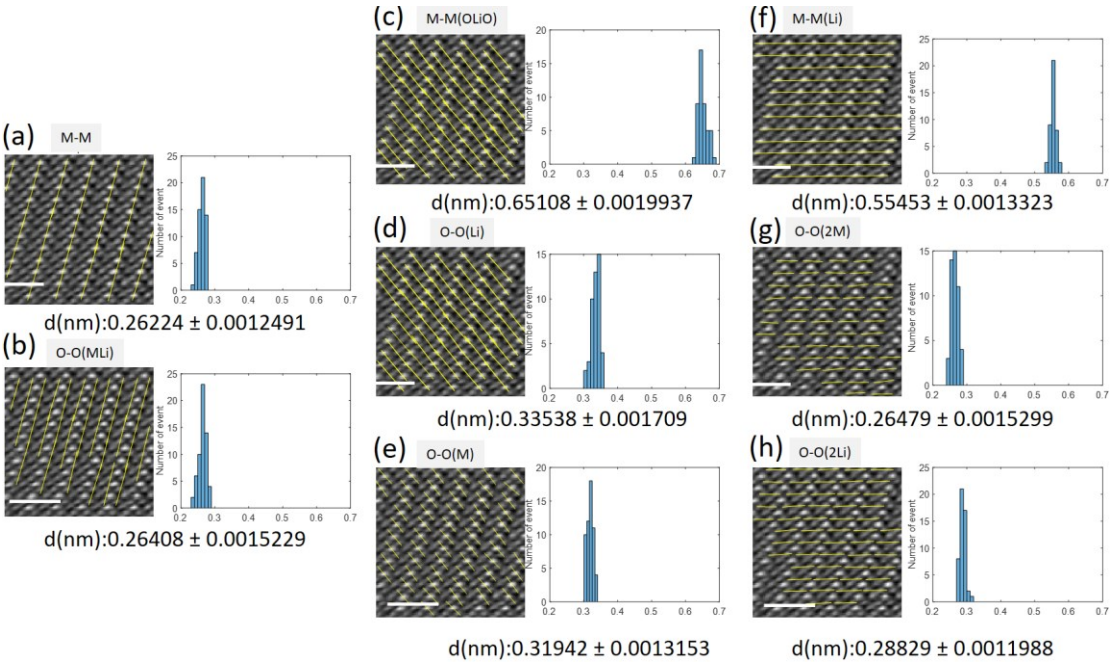

Figure S12. Ptychographic image of the bulk region of pristine $Li_{1.2}[Ni_{0.13}Mn_{0.54}Co_{0.13}]O_2$. The yellow lines in (a-h) illustrate the positions analysed by line profiling. The histogram shows the statistical results of the corresponding measured atom distance. Scale bar is 1 nm.

Table S1. Measured and calibrated atom distance.

Summary of the directly measured distances from the ptychographic phase image and calibrated values from a bulk region of pristine $Li_{1.2}[Ni_{0.13}Mn_{0.54}Co_{0.13}]O_2$. Unit is in nm.

Bulk	Measured	error	Calibrated	error
M-M	0.26224	1.25E-03	0.255	3.0E-03
O-O(MLi)	0.26408	1.52E-03	0.257	3.1E-03
M-M(OLiO)	0.65108	1.99E-03	0.601	4.3E-03
O-O(Li)	0.33538	1.71E-03	0.309	2.8E-03
M-M(Li)	0.55453	1.33E-03	0.520	3.3E-03
O-O(2M)	0.26479	1.53E-03	0.248	2.4E-03
O-O(2Li)	0.28829	1.199E-03	0.270	2.2E-03
O-O(M)	0.31942	1.315E-03	0.295	2.4E-03

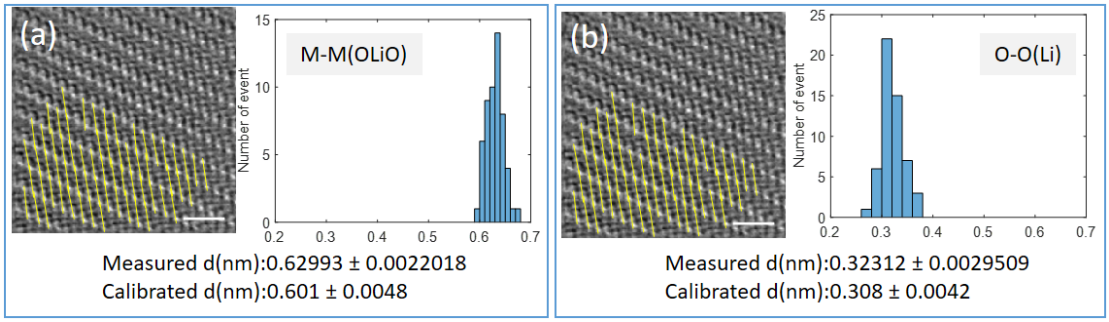

Figure S13. Ptychographic image of the bulk region of a second particle of pristine $Li_{1.2}[Ni_{0.13}Mn_{0.54}Co_{0.13}]O_2$ to evidence the reproducibility.

The line profiles in (a) and (b) are along the M-M(OLiO) direction. Although the direct measured values are difference from the first particle above, the calibrated results are close. Scale bar is 1 nm.

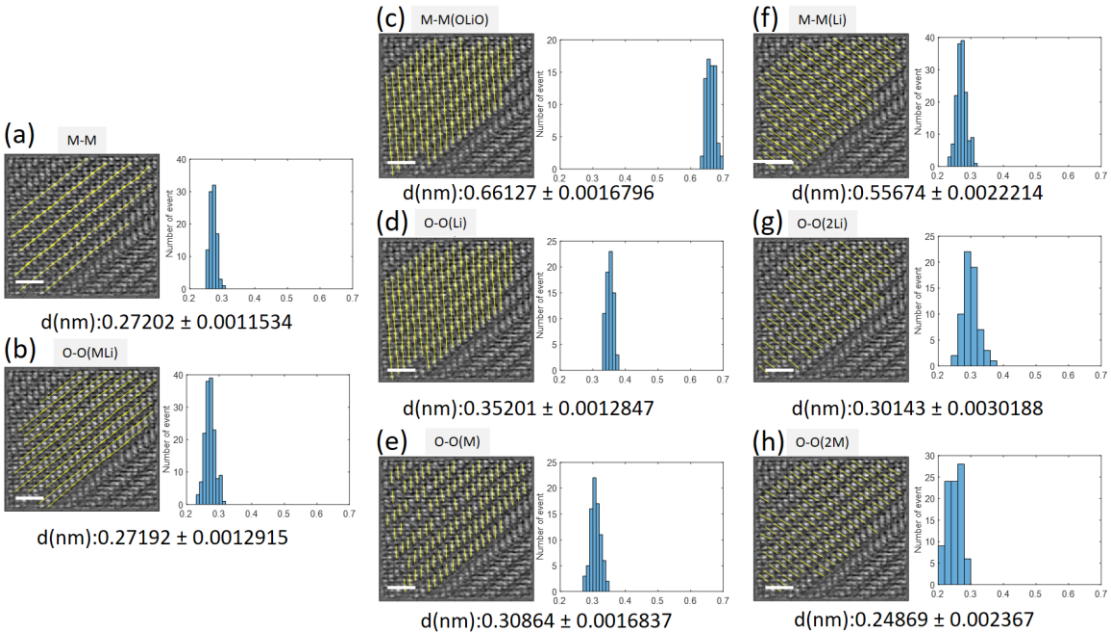

Figure S14. Ptychographic image of the bulk region of charged $Li_{1.2}[Ni_{0.13}Mn_{0.54}Co_{0.13}]O_2$. The yellow lines in (a-h) illustrate the positions analysed by line profiling. The histogram shows the statistical results of the corresponding measured atom distance. Scale bar is 1 nm.

Table S2. Measured and calibrated atom distance.

Summary of the directly measured distances from the ptychographic phase image and calibrated values from a bulk region of charged $Li_{1.2}[Ni_{0.13}Mn_{0.54}Co_{0.13}]O_2$. Unit is in nm.

Bulk	Measured	error	Calibrated	error
M-M	0.27202	1.15E-03	0.257	2.9E-03
O-O(MLi)	0.27192	1.29E-03	0.257	3.0E-03
M-M(OLiO)	0.66127	1.68E-03	0.611	4.1E-03
O-O(Li)	0.35201	1.28E-03	0.325	2.5E-03
M-M(Li)	0.55674	2.22E-03	0.537	5.8E-03
O-O(2M)	0.24869	2.37E-03	0.240	3.9E-03
O-O(2Li)	0.30143	3.02E-03	0.291	4.9E-03
O-O(M)	0.30864	1.68E-03	0.285	2.7E-03

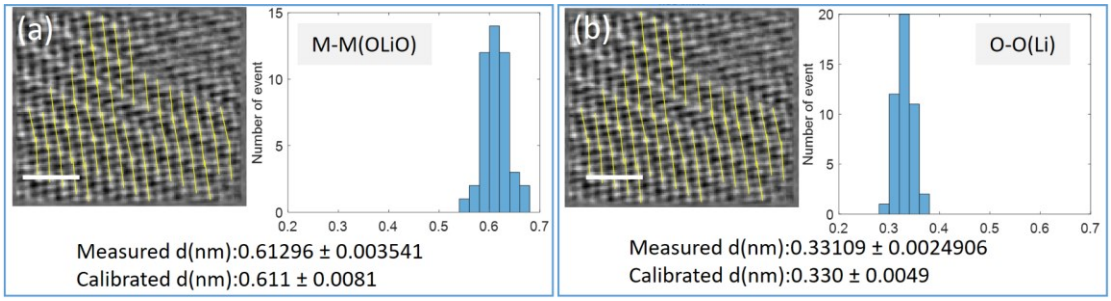

Figure S15. Ptychographic image of the bulk region of a second particle of charged $Li_{1.2}[Ni_{0.13}Mn_{0.54}Co_{0.13}]O_2$ to evidence the reproducibility.

The line profiles in (a) and (b) are along the M-M(OLiO) direction. Scale bar is 1 nm.

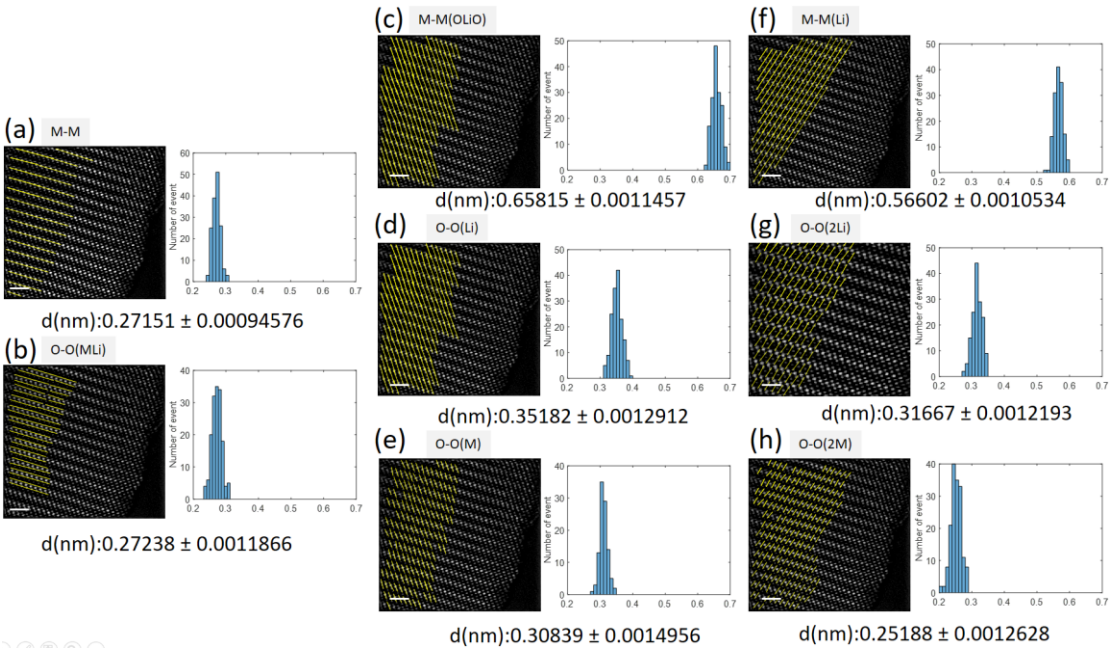

Figure S16. Ptychographic image of the bulk region of discharged $Li_{1.2}[Ni_{0.13}Mn_{0.54}Co_{0.13}]O_2$.

The yellow lines (a-h) illustrate the positions analysed by line profiling. The histogram shows the statistical results of the corresponding measured atom distance. Scale bar is 1 nm.

Table S3. Measured and calibrated atom distance.

Summary of the directly measured distances from the ptychographic phase image and calibrated values from a bulk region of discharged $Li_{1.2}[Ni_{0.13}Mn_{0.54}Co_{0.13}]O_2$. Unit is in nm.

Bulk	Measured	error	Calibrated	error
M-M	0.27151	9.46E-04	0.258	2.6E-03
O-O(MLi)	0.27238	1.19E-03	0.258	2.8E-03
M-M(OLiO)	0.65815	1.15E-03	0.604	8.8E-04
O-O(Li)	0.35182	1.29E-03	0.323	1.7E-03
M-M(Li)	0.56602	1.05E-03	0.526	2.7E-03
O-O(2M)	0.25188	1.26E-03	0.234	1.9E-03
O-O(2Li)	0.31667	1.22E-03	0.295	2.1E-03
O-O(M)	0.30839	1.50E-03	0.283	2.3E-03

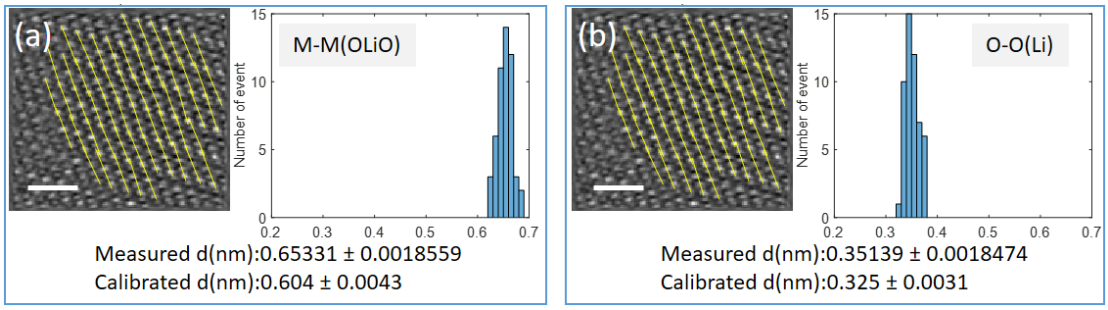

Figure S17. Ptychographic image of the bulk region of a second particle of discharged $Li_{1.2}[Ni_{0.13}Mn_{0.54}Co_{0.13}]O_2$ to evidence the reproducibility.

The line profiles in (a) and (b) are along the M-M(OLiO) direction. Scale bar is 1 nm.

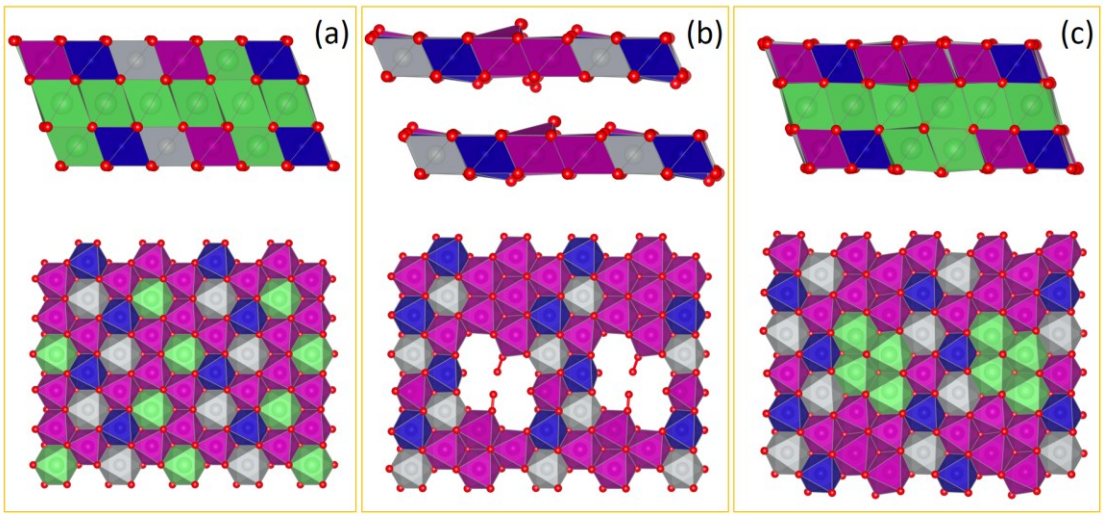

Figure S18. DFT calculation models for $Li_{1.2}[Ni_{0.13}Mn_{0.54}Co_{0.13}]O_2$.

(a) Pristine state. (b) Charged state. (c) Discharged state. In the models of each state, the upper row is projected view of the layered structure along the $[010]_{monoclinic}$ zone axis and below is the view of the transition metal layer along $[103]_{monoclinic}$ zone axis. The pristine model has a honeycomb cation ordering structure. In the charged model Co^{3+}/Ni^{2+} ions are fully oxidized to Co^{4+}/Ni^{4+} states, O_2 molecules are formed and caged in the TM vacancies that formed by in-plane TM migration. In the discharged model, all the O_2 molecules are reduced back to the O^{2-} ions, Co^{4+}/Ni^{4+} ions are reduced to Co^{3+}/Ni^{2+} states, all the TM layer and alkali layer vacancies are re-filled by Li^+ ions but some re-intercalated Li^+ ions occupy different sites from that in the pristine since the irreversible in-plane TM migration. In all models, the purple, blue, grey and green octahedra represent Mn, Co, Ni and Li in an octahedral coordination environment with O indicated by the red spheres.

Table S4. Atom distance from DFT.

Projected atom distance measured from the DFT model of pristine, charged (DFT_O_2 models), and discharged Li-rich NMC. The supercell is composed of 27 unit cells. Unit is nm.

DFT Bulk	Pristine	Charged	Percentage	Discharged	Percentage
M-M(OLiO)	0.582	0.597	2.7%	0.588	1.0%
O-O(Li)	0.309	0.333	7.7%	0.317	2.6%
O-O(M)	0.273	0.264	-3.1%	0.270	-0.8%
O-O (MLi)	0.251	0.253	0.6%	0.252	0.4%
O-O(2M)	0.233	0.218	-6.5%	0.235	0.9%

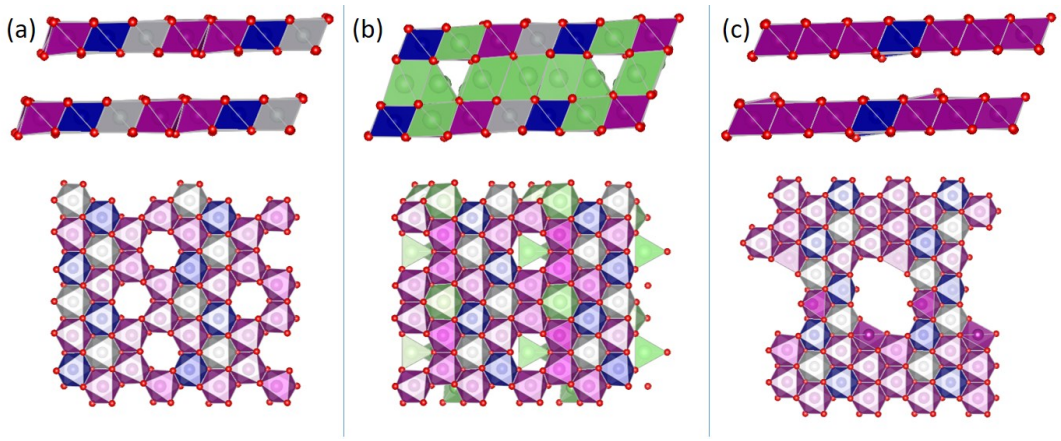

Figure S19. DFT calculation models of $Li_{1.2}[Ni_{0.13}Mn_{0.54}Co_{0.13}]O_2$ after oxidation along $[010]_{monoclinic}$ (top) and $[103]_{monoclinic}$ (bottom) zone axis.

(a) Model of electron hole states formed and the honeycomb cation ordering structure maintained, DFT_hole. (b) Model of pure TM oxidation, DFT_TM. (c) Model of O-deficient phase by removing the trapped O_2 molecules from the vacancy clusters (DFT_V_{O2}). Mn is represented in colour of purple, Co in blue, Ni in grey, Li in green and O in red.

Table S5. Atom distance from DFT.

Projected atom distance measured from the DFT model of pristine and charged Li-rich NMC (DFT_hole). The charged state models electron hole states formed and the honeycomb cation ordering structure maintained. The supercell is composed of 27 unit cells. Unit is nm.

DFT Bulk	Pristine	Charged	Percentage of change
M-M(OLiO)	0.582	0.598	2.8%
O-O(Li)	0.309	0.341	10.3%
O-O(M)	0.273	0.257	-5.7%
O-O (MLi)	0.251	0.249	-1.0%
O-O(2M)	0.233	0.213	-8.3%

Table S6. Atom distance from DFT.

Projected atom distance measured from the DFT model of pristine and charged Li-rich NMC (DFT_TM). The charged state models pure TM oxidation, that is Co^{3+}/Ni^{2+} ions are fully oxidized to the Co^{4+}/Ni^{4+} states. The supercell is composed of 27 unit cells. Unit is nm.

DFT Bulk	Pristine	Charged	Percentage
M-M(OLiO)	0.582	0.564	-3.0%
O-O(Li)	0.309	0.315	1.9%
O-O(M)	0.273	0.249	-8.7%
O-O (MLi)	0.251	0.250	-0.5%
O-O(2M)	0.233	0.221	-5.0%

Table S7. Atom distance from DFT.

Projected atom distance measured from the DFT model of pristine and charged Li-rich NMC (DFT_V_{O2}). The charged state models the trapped O_2 molecules in the vacancy clusters are removed. The supercell is composed of 27 unit cells. Unit is nm.

DFT Bulk	Pristine	Charged	Percentage
M-M(OLiO)	0.582	0.590	1.4%
O-O(Li)	0.309	0.333	7.6%
O-O(M)	0.273	0.257	-5.7%
O-O (MLi)	0.251	0.250	-0.5%
O-O(2M)	0.233	0.209	-9.9%

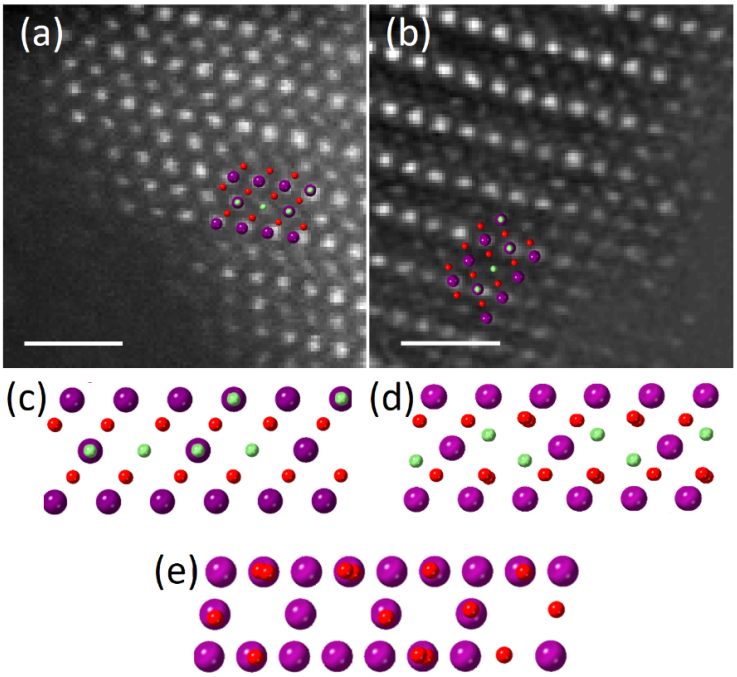

Figure S20. Surface reconstruction imaging.

HAADF images of the surface region of $Li_{1.2}[Ni_{0.13}Mn_{0.54}Co_{0.13}]O_2$ at (a) charged and (b) discharged states, respectively. Scale bar is 1 nm. Superposed crystal model is the LT-LCO type spinel. (c-e) Structural model of (c) LT-LCO type, (d) $LiMn_2O_4$ type and (e) Mn_3O_4 type spinel. The Li in LT-LCO spinel is at octahedral site while in $LiMn_2O_4$ type spinel at tetrahedral sites. In all crystal models, purple spheres represent TMs, red is O and green is Li.

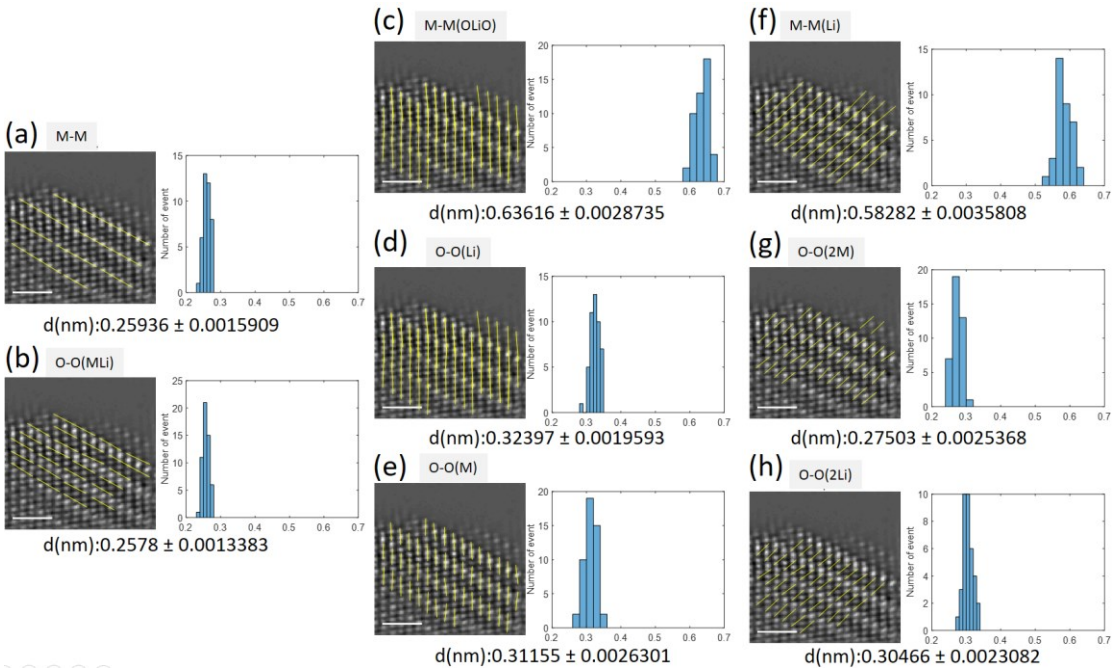

Figure S21. Ptychographic phase image of the surface region of pristine $Li_{1.2}[Ni_{0.13}Mn_{0.54}Co_{0.13}]O_2$.

The yellow lines in (a-h) illustrate the positions analysed by line profiling. The histogram shows the statistical results of the corresponding measured atom distance. Scale bar is 1 nm.

Table S8. Measured and calibrated atom distance.

Summary of the directly measured distances from the ptychographic phase image and calibrated values from a surface region of pristine $Li_{1.2}[Ni_{0.13}Mn_{0.54}Co_{0.13}]O_2$. Unit is in nm.

Surface	Measured	error	Calibrated	error
M-M	0.25936	1.59E-03	0.256	4.2E-03
O-O(MLi)	0.25780	1.34E-03	0.254	4.0E-03
M-M(OLiO)	0.63616	2.87E-03	0.600	6.7E-03
O-O(Li)	0.32397	1.96E-03	0.305	3.9E-03
M-M(Li)	0.58282	3.58E-03	0.520	7.8E-03
O-O(2M)	0.27503	2.5368E-03	0.245	4.5E-03
O-O(2Li)	0.30466	2.3082E-03	0.272	4.5E-03
O-O(M)	0.31155	2.63E-03	0.294	4.4E-03

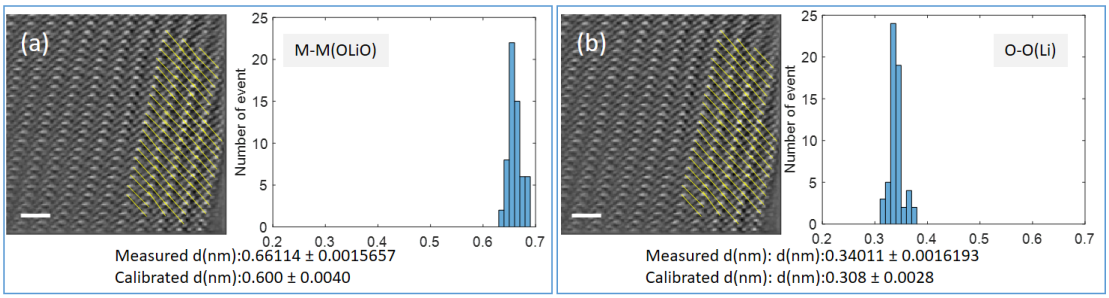

Figure S22. Ptychographic phase image of the surface region of a second particle of pristine $Li_{1.2}[Ni_{0.13}Mn_{0.54}Co_{0.13}]O_2$ to evidence the reproducibility.

The line profiles in (a) and (b) are along the M-M(OLiO) direction. Scale bar is 1 nm.

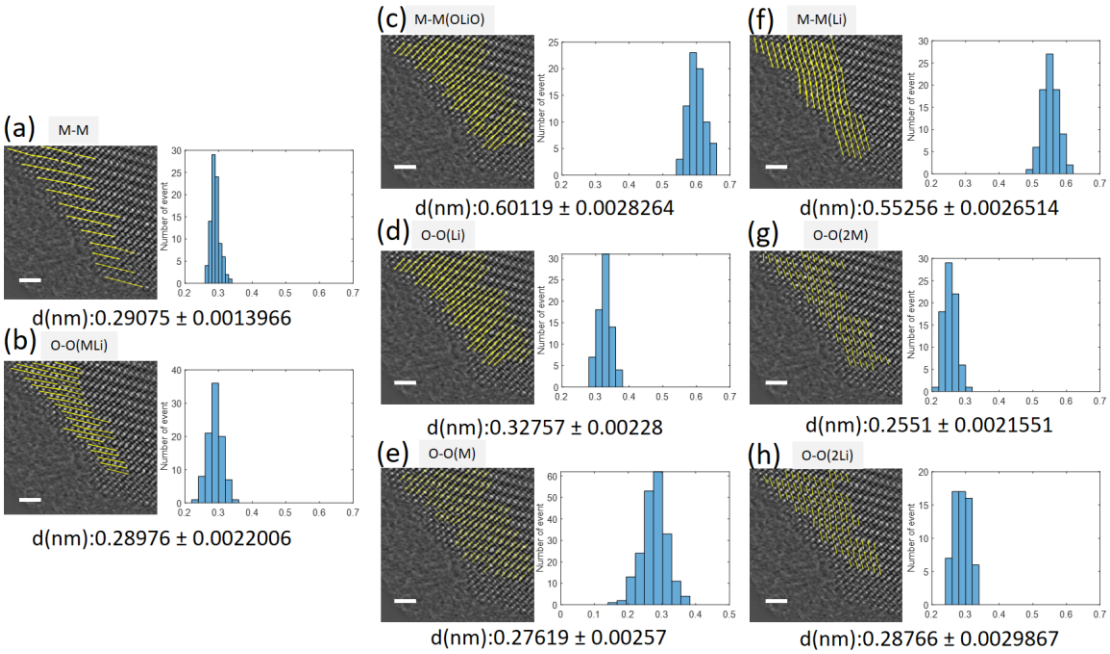

Figure S23. Ptychographic phase image of the surface region of charged $Li_{1.2}[Ni_{0.13}Mn_{0.54}Co_{0.13}]O_2$. The yellow lines in (a-h) illustrate the positions analysed by line profiling. The histogram shows the statistical results of the corresponding measured atom distance. Scale bar is 1 nm.

Table S9. Measured and calibrated atom distance.

Summary of the directly measured distances from the ptychographic phase image and calibrated values from a surface region of charged $Li_{1.2}[Ni_{0.13}Mn_{0.54}Co_{0.13}]O_2$. Unit is in nm.

Surface	Measured	error	Calibrated	error
M-M	0.29075	1.40E-03	0.263	3.2E-03
O-O(MLi)	0.28976	2.20E-03	0.262	3.9E-03
M-M(OLiO)	0.60119	2.83E-03	0.617	7.0E-03
O-O(Li)	0.32757	2.28E-03	0.336	4.6E-03
M-M(Li)	0.55256	2.65E-03	0.535	6.3E-03
O-O(2M)	0.25510	2.16E-03	0.247	3.8E-03
O-O(2Li)	0.28766	2.99E-03	0.278	4.8E-03
O-O(M)	0.27619	2.57E-03	0.283	4.6E-03

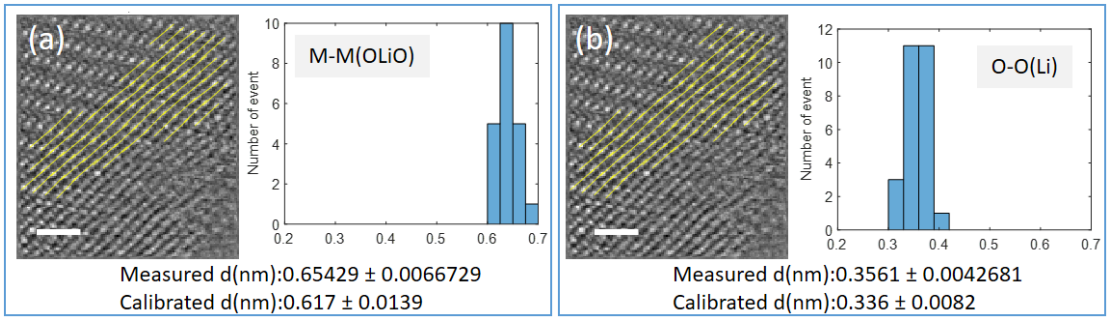

Figure S24. Ptychographic phase image of the surface region of a second particle of charged $Li_{1.2}[Ni_{0.13}Mn_{0.54}Co_{0.13}]O_2$ to evidence the reproducibility.

The line profiles in (a) and (b) are along the M-M(OLiO) direction. Scale bar is 1 nm.

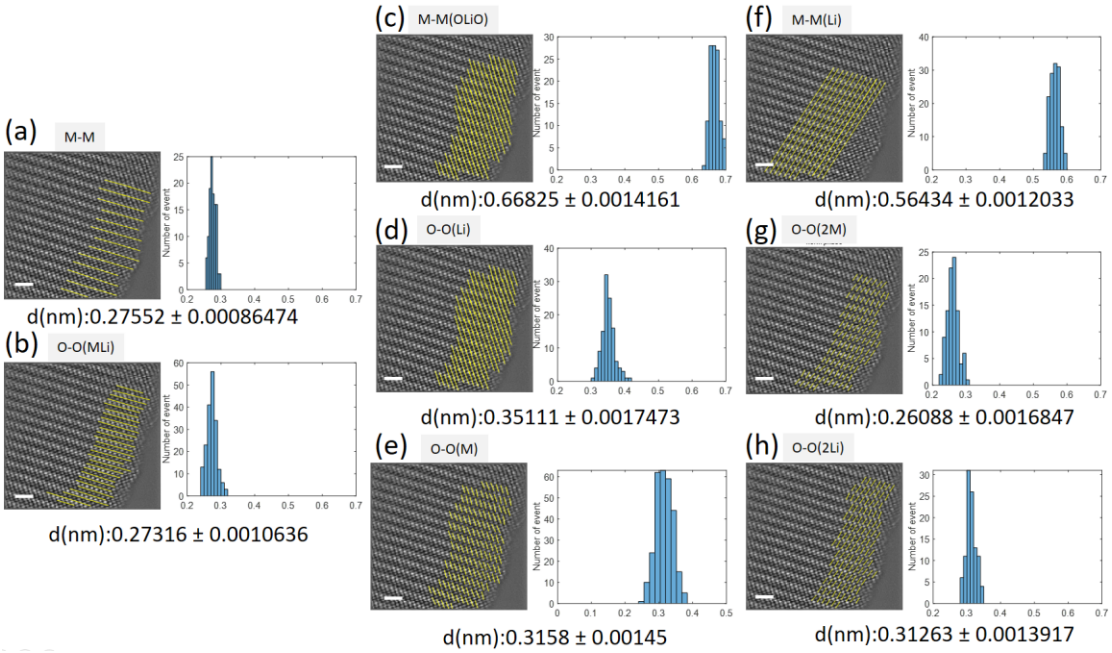

Figure S25. Ptychographic image of the surface region of discharged $Li_{1.2}[Ni_{0.13}Mn_{0.54}Co_{0.13}]O_2$.

The yellow lines in (a-h) illustrate the positions analysed by line profiling. The histogram shows the statistical results of the corresponding measured atom distance. Scale bar is 1 nm.

Table S10. Measured and calibrated atom distance.

Summary of the directly measured distances from the ptychographic image and calibrated values from a surface region of discharged $Li_{1.2}[Ni_{0.13}Mn_{0.54}Co_{0.13}]O_2$. Unit is in nm.

Surface	Measured	error	Calibrated	error
M-M	0.27552	8.65E-04	0.260	2.5E-03
O-O(MLi)	0.27316	1.06E-03	0.258	2.6E-03
M-M(OLiO)	0.66825	1.42E-03	0.608	3.8E-03
O-O(Li)	0.35111	1.75E-03	0.320	2.9E-03
M-M(Li)	0.56434	1.20E-03	0.531	3.0E-03
O-O(2M)	0.26088	1.68E-03	0.246	2.5E-03
O-O(2Li)	0.31263	1.39E-03	0.294	2.3E-03
O-O(M)	0.31580	1.45E-03	0.287	2.5E-03

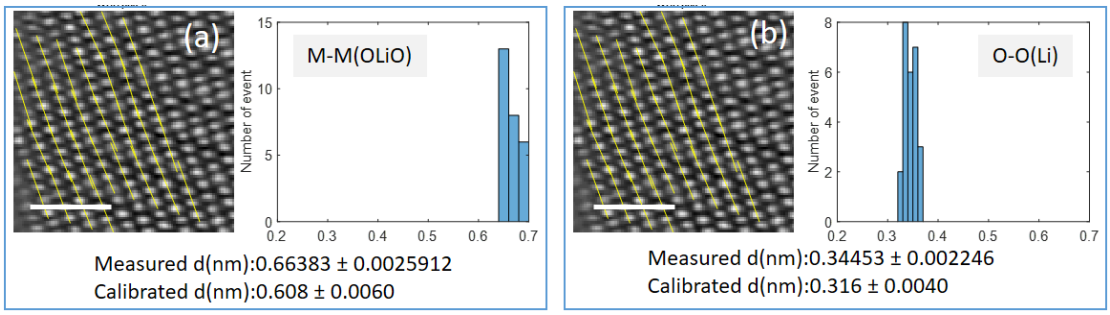

Figure S26. Ptychographic phase image of the surface region of a second particle of discharged $Li_{1.2}[Ni_{0.13}Mn_{0.54}Co_{0.13}]O_2$ to evidence the reproducibility.

The line profiles in (a) and (b) are along the M-M(OLiO) direction. Scale bar is 1 nm.

Supplemental Experimental Procedures

Measurement of zero-drift M-M distance from zero-drift ADF images

The HAADF images of $Li_{1.2}[Ni_{0.13}Mn_{0.54}Co_{0.13}]O_2$ were recorded using SmartAlign followed by rigid and non-rigid registration to generate zero-drift HAADF images. Figure S2a shows the zero-drift HAADF image of pristine $Li_{1.2}[Ni_{0.13}Mn_{0.54}Co_{0.13}]O_2$. The yellow lines denote the positions along M-M(OLiO) orientation in the defined bulk region where the line profiles are collected. The line profiles are positioned across the centre of mass of the atom columns, determined by using Gaussian filter in StatSTEM software. One of these line profiles, as displayed in Figure S2b identifies 11 peaks resulting from 11 atom columns across this line. In the exhibited line profile, the data points are fitted by the smoothspline program in MATLAB to optimize the atom column positions. The distance between two consecutive peaks is one result event in the statistical measurement. A number of the events generate the statistical result of the measurement on specific atom distance. Figure S2c displays the histogram of M-M(OLiO) distance from the direct measurement of the zero-drift HAADF image. The y axis in the histogram is the number of event at specific spacing. We can get the average and standard error from the histogram. Herein, the M-M(OLiO) in the bulk region of pristine $Li_{1.2}[Ni_{0.13}Mn_{0.54}Co_{0.13}]O_2$ is 0.59874 ± 0.00060097 nm. The average and standard error are used as reference to calibrate the measured results from ptychographic phase image. In the zero-drift HAADF images, we can also measure the named M-M and M-M(Li) atom distances.

Measurement of M-M and O-O distances from ptychographic images

Before correcting the drift in the atom distances measured from ptychographic phase image, we need to obtain the statistical results from the phase image. In the ptychographic phase image of the bulk region of pristine $Li_{1.2}[Ni_{0.13}Mn_{0.54}Co_{0.13}]O_2$, we first determine the M-M(OLiO) orientation combining with the analysis on the simultaneous ADF image. The lines are positioned across the centre of mass of the atom columns determined using StatSTEM. Figure S3a shows the M-M(OLiO) orientation.

One of the line profiles along M-M(OLiO) is displayed in Figure S3b where the five peaks denote the atom columns of TM, O, Li, O and TM, respectively. The spacing between the two peaks of TM columns is one event of the measured M-M(OLiO) distance and the spacing between the two O columns is one event of the measured O-O(Li) distance. Through the statistical measurement of all the labelled line profiles, the histograms of the M-M(OLiO) and O-O(Li) are plotted in Figure S3c and d respectively. The average and standard error is 0.65108 ± 0.0019937 nm for M-M(OLiO) and 0.33538 ± 0.001709 nm for O-O(Li).

Calibration of the measured distances from ptychographic images

The directly measured atom distances from ptychographic phase images contain errors resulting from sample drift. To correct the error, we carry out calibration using the reference obtained from zero-drift HAADF image. In the example, we use the statistical M-M(OLiO) distance from zero-drift HAADF, namely M-M(OLiO)_ADF to calibrate the M-M(OLiO) distance from ptychographic phase image, namely M-M(OLiO)_phase. The ratio between the two values is:

$$\text{ratio} = \frac{\text{M-M(OLiO)\_ADF}}{\text{M-M(OLiO)\_phase}} = \frac{0.59874 \pm 0.000601}{0.65108 \pm 0.0019937} = 0.919 \pm 0.003$$

The zero-drift M-M(OLiO) distance from the phase image is:

$M\text{-}M(OLiO)_{phase\_calibration} = M\text{-}M(OLiO)\_{phase} \times ratio = 0.598 \pm 0.004$ nm

The O-O(Li) is along the same orientation as M-M(OLiO), its drift is corrected using the ratio above calculated for M-M(OLiO). The zero-drift O-O(Li) distance from the phase image is:

$O\text{-}O(Li)_{phase\_calibration} = O\text{-}O(Li)\_{phase} \times ratio = 0.308 \pm 0.002$ nm

Following the same method, the zero-drift M-M and M-M(Li) distances from HAADF are used as references to calibrate the M-M and M-M(Li) distances measured from the phase image and the ratio between them is used to calibrate the O-O distances at the same orientation. In the named geometry of atom distance, O-O(MLi) is along the same orientation as M-M, O-O(2Li) and O-O(2M) are at the same orientation as M-M(Li).